polysaccharides

MDPI

Article

Chitosan–κ-Carrageenan–Lysozyme Nanoparticles Disrupt Appressorium Formation and Cellular Architecture in *Colletotrichum siamense* with Low Sensitivity to Chitosan

Alma Carolina Gálvez-Iriqui [1,*], Itzia Itzel Hoyos-Verdugo [1], Waldo Manuel Argüelles-Monal [2], Aaron de Jesús Rosas-Durazo [3], Armando Burgos-Hernández [1], Ana Karenth López-Meneses [1] and Maribel Plascencia-Jatomea [1,*]

[1] Microbiology and Mycotoxins Laboratory, Departamento de Investigación y Posgrado en Alimentos, Universidad de Sonora, Edificio 5P, Bulevar L.D. Colosio y Conocimiento S/N, Col. Centro, Hermosillo 83000, Sonora, Mexico; a214200847@unison.mx (I.I.H.-V.); armando.burgos@unison.mx (A.B.-H.); anakarenth.lopez@unison.mx (A.K.L.-M.)
[2] Biopolymer Laboratory, Centro de Investigación y Desarrollo en Alimentación A.C, Carretera Gustavo Enrique Astiazarán Rosas, No. 46, Hermosillo 83304, Sonora, Mexico; waldo@ciad.mx
[3] Departamento de Metal Mecánica, Instituto Tecnológico de Hermosillo, Av. Tecnológico 115, Col. Sahuaro, Hermosillo 83170, Sonora, Mexico; a.rosas.durazo@gmail.com
* Correspondence: alma.galvez@unison.mx (A.C.G.-I.); maribel.plascencia@unison.mx (M.P.-J.); Tel.: +526-624333452 (A.C.G.-I.); +52-6625922-09 (M.P.-J.)

Abstract

Colletotrichum species are among the most destructive phytopathogens worldwide, with appressorium-mediated penetration representing a critical stage in host infection. Targeting this morphogenetic transition offers a promising strategy for sustainable disease control by interfering with the infection process rather than solely inhibiting fungal growth. In this study, chitosan–κ-carrageenan nanoparticles (CS–κ-CRG) without and with lysozyme (CS–κ-CRG/Lz) were synthesized, characterized, and evaluated for their ability to inhibit appressorium formation in *Colletotrichum siamense*, a strain exhibiting low sensitivity to chitosan. The nanoparticles showed monodisperse size distributions, with hydrodynamic diameters of 503 and 333 nm for CS–κ-CRG and CS–κ-CRG/Lz, respectively, positive surface charges of approximately +26 mV, spherical morphology, and a lysozyme encapsulation efficiency of 63%. Both formulations significantly reduced conidial viability and delayed germination, inducing morphological alterations such as conidial swelling, hyphal deformation, and vacuolization. Fluorescence microscopy using calcofluor white and propidium iodide revealed disturbances in cell wall organization and loss of membrane integrity. Both nanomaterials markedly affected appressorium development in a concentration- and formulation-dependent manner. Notably, CS–κ-CRG/Lz showed stronger suppression of appressorium formation, whereas at 200 μg·mL^{-1}, CS–κ-CRG nanoparticles stimulated appressorium formation, suggesting that sublethal nanoparticle stress may trigger compensatory or hyper-pathogenic responses. These findings highlight the potential and complexity of utilizing chitosan-based nanomaterials for phytopathogen management and emphasize the importance of mechanistic and dose–response evaluations before field application.

Keywords: biopolymer nanocomposites; antifungal activity; fungal morphogenesis

Check for updates

Academic Editor: Philippe Michaud

Received: 16 February 2026
Revised: 18 March 2026
Accepted: 22 April 2026
Published: 30 April 2026

Copyright: © 2026 by the authors. Licensee MDPI, Basel, Switzerland. This article is an open access article distributed under the terms and conditions of the Creative Commons Attribution (CC BY) license.

1. Introduction

Colletotrichum is one of the most economically significant genera of phytopathogenic fungi worldwide, responsible for anthracnose diseases in a wide range of commercially important fruits, vegetables, and ornamentals. Infections with these pathogens occur in both pre- and postharvest stages, leading to substantial yield losses, quality deterioration, and reduced shelf life, particularly in perishable commodities such as mango, avocado, papaya, berries, and peppers [1–3]. Their ability to produce specialized infection structures, including appressoria with high turgor pressure, enables efficient host penetration and rapid disease progression [4,5]. Moreover, the taxonomic complexity and genetic diversity of *Colletotrichum* species complicate disease diagnosis and management, contributing to the persistence of outbreaks [6]. Due to its impact on global food supply chains and postharvest security, *Colletotrichum* spp. remains a critical target for developing innovative, sustainable disease-control strategies. To ensure successful control of phytopathogenic fungi, such as *Colletotrichum* spp., the integrated pest management of biological, physical, and chemical alternatives with low environmental impact has been incorporated, such as plant extracts, pure or mixtures of secondary metabolites, and essential oils, as well as biopolymers like chitosan and antimicrobial enzymes from various sources [7,8]. Lysozyme is an antimicrobial enzyme that hydrolyzes β-1,4-glycosidic bonds in peptidoglycan, leading to cell wall disruption in susceptible microorganisms; moreover, lysozymes and lysozyme-like enzymes from various natural sources have been shown to interact with fungal cell wall polysaccharides (such as glucans or chitin), which can alter their integrity and generate stress [9–11]. Incorporating lysozymes and lysozyme-like enzymes into chitosan-based nanomaterials has gained relevance as a combined strategy for microbial control, as the synergistic interaction between chitosan's polycationic properties and lysozyme's enzymatic activity enhances permeability and structural damage in microbial cells [12–14]. Enzyme immobilization could increase its antimicrobial activity and prolong their effectiveness [9,14,15].

Furthermore, polyelectrolyte complexes based on chitosan and carrageenan have been successfully synthesized and used to address technological challenges [12,16]. Recently, chitosan-based nanomaterials have been proposed to control the in vitro growth of *Colletotrichum musae*, *Colletotrichum chrysophillum*, *Colletotrichum fruticola*, *Colletotrichum gloeosporioides*, and *Colletotrichum siamense* [8,17,18]. Additionally, Hernandez-Téllez et al. [19] reported the activity of chitosan–carrageenan–lysozyme nanomaterials to inhibit the germination of conidia and metabolic activity (i.e., the initial growth stages) of *Aspergillus parasiticus*, thereby interfering with the development of key barrier structures through effects on cell wall synthesis and plasma membrane integrity. Although these studies highlight the promising potential of chitosan-based nanomaterials such as chitosan–carrageenan–lysozyme, its potential to control phytopathogenic fungi such as *Colletotrichum* spp. has not been explored, and none have examined their effects on specific morphogenetic events such as appressorium differentiation, leaving an important knowledge gap and a valuable opportunity for innovation in the control of phytopathogenic fungi.

Appressoria are specialized structures produced by various filamentous fungi to adhere and penetrate host tissues, thereby facilitating infection and colonization. These differentiated cells generate high mechanical pressure and secrete lytic enzymes that degrade physical barriers, making them a critical point in the establishment of pathogenicity [5]. Controlling appressorium development using nanotechnology approaches has emerged as a promising strategy, as these nanomaterials—mainly metallic nanoparticles—can interfere with adhesion, the formation of penetration structures, and fungal cell wall integrity [20,21]. Notwithstanding the significance of this specific structure in host invasion and disease manifestation, its association with antifungal chitosan-based nanoparticles remains un-

known. This study aimed to synthesize chitosan–carrageenan–lysozyme nanoparticles and evaluate their effects on appressorium formation and fungal growth in the phytopathogenic fungus *Colletotrichum siamense*, a species reported to exhibit relatively low sensitivity to chitosan-based treatments. The research examines early infection-related morphogenesis through metabolic viability assays, morphometric assessment, and fluorescence microscopy to characterize structural and developmental changes in fungal cells and appressoria. In addition to inhibitory effects, this study also explores the stimulation of appressorium differentiation at intermediate nanoparticle concentrations. By assessing these responses at the level of infection structure formation, this work provides new insights into how chitosan-based nanomaterials interact with mechanisms driving fungal pathogenicity.

2. Materials and Methods

2.1. Reagents and Materials

Commercial chitosan (CS) with medium molecular weight was purchased from Sigma-Aldrich (CAS: 9012-76-4, LOT# MKBD7238V, St. Louis, MO, USA). κ-Carrageenan with 28% sulfate content was provided by CarboMer Inc. (Lot No. 07-S082A, San Diego, CA, USA) and used without any purification. Commercial lysozyme from chicken egg white (lyophilized powder, protein $\geq$ 90%, $\geq$40,000 units/mg protein) was purchased from Sigma-Aldrich (Saint Louis, MO, USA). Glacial acetic acid (99% purity) was purchased from JT Baker (Center Valley, PA, USA). A fluorescent brightener (Calcofluor white) and propidium iodide (>94% purity) dyes were purchased from Sigma-Aldrich (St. Louis, MO, USA). Tetrazolium salt XTT (2,3-bis (2-methoxy-4-nitro-5-sulfophenyl)-2-h-tetrazolium-5-carboxanilide bromide) and menadione were purchased from Sigma-Aldrich (St. Louis, MO, USA). Commercial synthetic fungicide flutriafol: (RS)-2,4′-difluoro-α-(1H-1,2,4-triazol-1-ylmethyl) benzyl alcohol at 11.80% ($w{\cdot}w^{-1}$) was purchased from Chemionova (Lemving, Denmark).

2.2. Biological Cultures

A *Colletotrichum siamense* strain previously isolated from mango leaf infected with anthracnose was provided by the Plant Physiology Laboratory of CIAD, A.C., Hermosillo. The molecular identification was previously carried out using a multi-locus sequence analysis scheme based on five genes (actin, Act; beta-tubulin 2, β-Tub2; glyceraldehyde-3-phosphate dehydrogenase, GAPDH; chitin synthase 1, CHS-1; calmodulin, CaM) and the ribosomal internal transcribed spacer (ITS) and Apn2-Mat1-2 (ApMat) intergenic spacer region. This phytopathogen was identified as a fungus with low sensitivity to chitosan [8,22].

2.3. Partial Characterization of Chitosan, κ-Carrageenan and Lysozyme

2.3.1. Chitosan and κ-Carrageenan

Prior to use, viscosimetric molecular weight (Mv) and the deacetylation degree (DD%) of commercial chitosan (CS) were examined via viscosity measurement and conductimetric titration [23]. The sulfate content of κ-carrageenan (κ-CRG) was previously examined and reported by [24].

2.3.2. Lysozyme Activity

Lysozyme activity was assessed using dry biomass of *Micrococcus lysodeikticus* as a substrate based on the method of [25,26]. First, a 0.1 mL aliquot of the enzyme suspension was added to 2.5 mL of 0.3 mg·mL^{-1} dry cell suspension in 100 mM phosphate buffer (pH 6.2). Next, the enzymatic activity was measured during the first 2 min of linear decrease in absorbance at 450 nm at 25 $\pm$ 1 °C using a UV-visible spectrophotometer from ThermoFisher (Model BIOMATE 3S, Madison, WI, USA). One unit of lysozyme activity was defined as the quantity which caused a 0.001/min decrease in absorbance of *M. lysodeikticus*

suspended in 100 mM phosphate buffer at pH 6.2. The enzyme activity was measured using different concentrations, ranging from 0 to 0.5 mg·mL^{-1}, in order to select the concentration capable of reducing the turbidity of the substrate by 50% (IC_{50}). This concentration was used in subsequent assays.

2.3.3. Effect of pH and Stability on Lysozyme Activity

The lysozyme activity was determined at different pH values, ranging from 2 to 8. For each pH, 250 mL of buffer solution was prepared with 0.1 M H_3PO_4-KCl (pH 2–3), 0.1 M H-COOH-KCl (pH 3.5), 0.1 M CH_3COOH-KCl (pH 4–5.5), 0.1 M Na_2HPO_4-NaH_2PO4 (pH 6–7.5), and 0.1 M EDTA-NaOH (pH 8). The buffers were used to dilute an *M. lysodeikticus* stock suspension of 6 mg·mL^{-1} in water at a final concentration of 0.3 mg·mL^{-1}. The lysozyme activity was measured at 450 nm, and the results are expressed as a percentage of the highest activity measured in this experiment. For pH stability, different lysozyme solutions were prepared at 0.08 mg·mL^{-1} with pH values ranging from 2 to 8, and all buffers had an ionic strength of 0.1. All lysozyme solutions were incubated for 120 h at 25 °C using a low-temperature refrigerated incubator (Model TE-I45DM, Guadalajara, Jalisco, Mexico). Before measurements, the pH was adjusted to 6.2. Lysozyme activity was measured each 24 h. The results are expressed as a percentage of the highest activity measured in this experiment [26].

2.4. Synthesis of Chitosan-Carrageenan-Lysozyme (CS–κ-CRG/Lz) Nanoparticles

2.4.1. Biopolymers Preparation

A solution of CS was prepared by dissolving 0.05 g of dry flakes in 100 mL of aqueous 0.5% (*w*/*w*) acetic acid solution. Additionally, 0.5% (*w*/*w*) of Tween 80 was added as a surfactant. The mixture was maintained under constant magnetic stirring for 24 h at room temperature until the biopolymer was completely dissolved. κ-Carrageenan (κ-CRG) solution was prepared by dissolving it in ultra-pure water to a final concentration of 1 mg·mL^{-1}.

2.4.2. Synthesis

CS–κ-CRG nanoparticles loaded and not loaded with lysozyme were synthesized by ionic complexation [19,27]. First, 1 mL of κ–CRG solution at 0.5 mg·mL^{-1} was added drop-by-drop using a peristaltic pump to 4 mL of CS solution at 0.5 mg·mL^{-1} under magnetic stirring at 500 rpm. For CS–κ-CRG nanoparticles loaded with lysozyme, 1 mL at 1 mg·mL^{-1} of lysozyme was first added drop-by-drop to the CS solution. Then, the step was repeated using 1 mL of κ-CRG solution at 0.5 mg·mL^{-1}. The final pH value was 5.6. For physical–chemical and biological characterization, the nanoparticles were freshly synthesized.

2.5. Physicochemical Characterization of CS–κ-CRG/Lz Nanoparticles

2.5.1. Average Size, ζ-Potential, and Polydispersity Index

The average size, dispersion, and ζ-potential of the nanoparticles were measured by dynamic light scattering (DLS) using a Zetasizer Nano ZS equipment (Malvern Instruments Ltd., Malvern, Worcestershire, UK). First, 1 mL was placed in the equipment cell using a clean syringe. The detection angle was maintained at 173° and at least three replicates were obtained at 25 ± 1 °C. The experimental data were analyzed employing an automated particle characterization system from Malvern Zetasizer Software Version 7.13.

2.5.2. Morphology of CS–κ-CRG/Lz Nanoparticles by Atomic Force Microscopy (AFM) and Transmission Electron Microscopy (TEM)

For AFM examination, 100 µL of solution of the liquid samples of CS–κ-CRG and CS–κ-CRG/Lz nanoparticles was deposited via spin-coating to silica sheets measuring 1 cm^2. Thereafter, the samples were dried at ambient conditions prior to analysis. AFM measurements were performed using a multimode scanning probe microscope (Bruker Nano Surfaces and Metrology, Santa Barbara, CA USA) with NanoScope III controller at 1 Hz scanning range operating in tapping mode. The TEM examination was performed using a JEM 2010F transmission electron microscope with operating voltage of 200 kV (JEOL, Ltd., Tokyo, Japan) and the liquid samples of CS–κ-CRG and CS–κ-CRG/Lz nanoparticles underwent lyophilization for drying. Thereafter, a small portion of the sample was placed on a carbon/nickel grid. Subsequently, the samples were incubated for 12 h under vacuum conditions. Images from different points on the sample were captured for both studies [28].

2.5.3. Encapsulation Efficiency and Lysozyme Loading Capacity

The lysozyme encapsulation efficiency and loading capacity of the CS–κ-CRG matrix were determined from the residual amount of Lz in the supernatant [19]. Lz was previously obtained via centrifugation of the CS–κ-CRG/Lz sample. The centrifugation conditions used were 13,500 rpm, 1.5 h, and 4 °C using a Centrifuge 5804 R (Eppendorf, Hamburg, Germany). For lysozyme quantification, the protein micro-BCA assay kit was used (Pierce, Thermo Fisher Scientific, Madison, WI, USA). Serum bovine albumin was used as standard. The absorbance was measured at 530 nm using a microplate reader (FLUOstar 415-2094, BMG LABTECH Inc., Ortenberg, Germany). The encapsulation efficiency (EE) and loading capacity (LC) of nanoparticles were determined according to [19,29], using Equations (1) and (2):

$$\text{Encapsulation efficiency (EE, \%)} = \left(\frac{\textit{Total lysozyme added} - \textit{Free lysozyme not trapped}}{\textit{Total lysozyme added}} \right) \times 100 \quad (1)$$

$$\text{Loading capacity (LC, \%)} = \frac{\textit{Amount of lysozyme in the particles}}{\textit{Total weight of charged nanoparticles}} \times 100 \quad (2)$$

2.5.4. Infrared Spectroscopy

CS–κ-CRG and CS–κ-CRG/Lz nanoparticles samples were analyzed via FT-IR (FT-IR Spectrum GX, Perkin-Elmer, Shelton, CT, USA), employing the attenuated total reflection (ATR) accessory. The FT-IR spectrum of freshly prepared particles at a concentration of 1 $mg{\cdot}mL^{-1}$ was obtained in a liquid medium (water). Measurements were performed at room temperature, and an average of 16 scans in a spectral range of 4000–400 cm^{-1} were recorded [30,31].

2.6. Antifungal Activity of CS–κ-CRG and CS–κ-CRG/Lz Nanoparticles Against Colletotrichum siamense

2.6.1. Conidial Viability by Colorimetric XTT Assay

In a 96-well microplate, 100 µL of *C. siamense* suspension (2×10^6 conidia/mL) were added in triplicate. Subsequently, an aliquot of 100 µL from each treatment of CS–κ-CRG nanoparticles, CS–κ-CRG/Lz nanoparticles, lysozyme, and flutriafol at concentrations of 300, 200, 90, 40, and 0 $\mu g{\cdot}mL^{-1}$ were introduced to each well. The microplate was incubated for 4 h at 28 ± 2 °C. Sterile distilled water at neutral pH and acidified water at pH 5.6 were used as controls. Then, a volume of 57 µL of a solution mixture of XTT (2 $mg{\cdot}mL^{-1}$) and menadione (1 mM) was added to each well. The microplate was incubated for another 8 h

under the same conditions. Finally, the absorbance was measured at 450 nm using an ELISA plate reader at 8 and 12 h of incubation (Model iMark, BIO-RAD, Hercules, CA, USA) [30]. The results are expressed as a conidial viability percentage with respect to acidified water control. The experimental data were analyzed using a Probit survival/reliability test (NCSS ver. 10 statistical software, NCSS LLC, Kaysville, UT, USA) to obtain the concentrations that inhibited 50% of the conidia viability (IC_{50}). Subsequent experiments were conducted at 200 and 330 $\mu g \cdot mL^{-1}$, concentrations selected based on the IC_{50} values estimated for CS–κ-CRG and CS–κ-CRG/Lz nanoparticles.

2.6.2. Germination of Conidia and Kinetic Parameters

A 7-day-old *C. siamense* monosporic culture grown at 26 ± 2 °C was used to prepare a conidia suspension at 2×10^5 conidia/mL using sterile Czapek broth at 0.1% (*w*/*v*) of Tween 80. Next, 750 µL of conidia suspension was added to a 12-well plate along with 750 µL of each treatment (CS–κ-CRG and CS–κ-CRG/Lz nanoparticles), and then incubated in darkness at 28 ± 2 °C. Randomized sampling was performed at 0, 6, 12, 16, 18, and 24 h of incubation, during which 200 conidia (germinated and non-germinated) were examined using an optical microscope (Model CX311RTSF, Olympus, Tokyo, Japan) [30]. The experimental data are expressed as germinated conidia (%) versus time. Subsequently, the data were adjusted to the logistic kinetic model using Equation (3):

$$S(\%) = \frac{smax}{1 + \frac{Smax - S0}{S0} \times e^{-kt}} \quad (3)$$

where S is the percentage of germinated conidia after a given time (t), S_{max} is the maximal percentage of conidia germinated when $t \to \infty$, S_0 is the initial percentage of conidia germinated (at t = 0), and *k* is the germination rate (h^{-1}) [30].

2.6.3. Morphometric Analysis

The changes in the width and length of conidia, hyphae, and appressoria during the germination process were assessed using the Image Pro Plus 6.3 software (Media Cybernetics, Inc., Bethesda, MD, USA). The measurements were taken at 12, 16, 18, and 24 h of the incubation period (28 ± 2 °C) for the normal growth control (pH 7 and 5.6), CS–κ-CRG nanoparticles (200 and 330 $\mu g \cdot mL^{-1}$), and CS–κ-CRG/Lz nanoparticles (200 and 330 $\mu g \cdot mL^{-1}$), respectively. Additionally, images from each treatment were taken at 40× using unstained bright-field microscopy (Model CX311RTSF, Olympus, Tokyo, Japan) [18,30].

2.6.4. Appressorium Formation

Appressorium formation was evaluated at concentrations of 200 and 330 $\mu g \cdot mL^{-1}$, selected according to the IC_{50} values estimated from conidial viability assays for CS–κ-CRG and CS–κ-CRG/Lz nanoparticles. A microscopic analysis was performed, counting 200 appressoria for each nanoparticle treatment and the normal growth control at 12, 16, 18, and 24 h during the germination process; the results are represented as a percentage of appressorium production [32].

2.6.5. Effect on Cell Membrane Integrity and Cell Wall

A sterile glass slide was placed at the bottom of each well of a 12-well microplate. Afterwards, 750 µL of a suspension containing 2×10^5 conidia/mL was applied to each well. The concentrations of CS–κ-CRG and CS–κ-CRG/Lz nanoparticles utilized were 200 and 330 $\mu g \cdot mL^{-1}$, respectively. Next, 750 µL of a sample was added to each well of a 12-well plate, with three replicates for each treatment. Subsequently, the microplate was

subjected to an incubation period of 12 h at a temperature of 28 ± 2 °C. Following this, the glass slides containing the fungal growth were taken out and treated with fluorescent dyes [30].

To confirm cell membrane integrity, two drops of propidium iodide (PI) at a concentration of 3 μM (*w*/*v*) were added to the conidia growth, and the samples were incubated at 4 °C for 15–30 min. In addition, 10 $\mu g \cdot mL^{-1}$ of Fluorescent Bright (Calcofluor white) was added to the conidia growth to assess cell wall integrity. Subsequently, the samples were incubated for 15 to 30 min at 4 °C in the dark. Observations were carried out using an inverted microscope (Model DMi8, Leica Microsystems, Wetzlar, Germany) equipped with fluorescence filters (546/10 RHOD excitation filter and 585/40 emission, 350/50 DAPI excitation filter and 460/40 emission, and 480/40 excitation FITC filter and 527/30 emission), a cooled monochromatic DFC 450C camera (Leica Microsystems, Wetzlar, Germany), and fluorescence overlay software (LAS AF ver. 3.1.0, Leica Microsystems CMS GmbH, Mannheim, Germany).

2.7. Statistical Analysis

A completely randomized design was carried out using one-way analysis of variance (ANOVA) at a significance level set at $p \leq 0.05$. Means for homogeneous groups were assessed using the Tukey post hoc test at a 95% confidence interval. Differences were accepted as significant when $p \leq 0.05$ (OriginPro 9.1 SR0, v8.0724). All data are presented as the means ± SEM.

3. Results and Discussion

3.1. Partial Characterization of Chitosan, κ-Carrageenan, and Lysozyme as Nanoparticle Components

3.1.1. Physicochemical Features of Chitosan and κ-Carrageenan

The viscosimetric molecular weight (Mv) and deacetylation and acetylation degree of commercial chitosan (CS) were examined using viscosity measurement and conductimetric titration [23]. The Mv was 105.8 kDa with deacetylation and acetylation degrees of 67.6 ± 2.9% and 32.45 ± 2.89%, respectively. The observed Mv and DD% correspond, according to the literature, to low molecular weight and a low degree of chitosan deacetylation. These characteristics influence nanoparticle formation, cellular surface interactions, biodegradation, and even toxicity [8,19,33,34]. The κ-carrageenan polymer used in this study was previously characterized and has been reported to have the capacity to create polyelectrolytic complexes with surfactants [24]. The sulfate in κ-CRG can interact with the amino groups in CS to form a polyelectrolytic complex which is held together by electrostatic forces, allowing the production of a polyelectrolyte polymeric complex which is suitable for enzyme immobilization [19,27,35–37].

3.1.2. pH-Dependent Lysozyme Activity and Stability

In the present study, commercial lysozyme derived from chicken egg white had significant enzymatic activity in a mildly acidic pH range of 5.5–6.5, as evidenced by the *Micrococcus lysodeikticus* assay (Figure 1a). Muramidase activity was consistently high at pH 5.5 to 6.25 (≥80%), and the enzyme maintained its activity for over 120 h under these conditions (Figure 1b). At pH 5.5, lysozyme stability diminished over the initial 48 h, indicating that mildly acidic environments may cause subtle structural alterations that impact long-term stability.

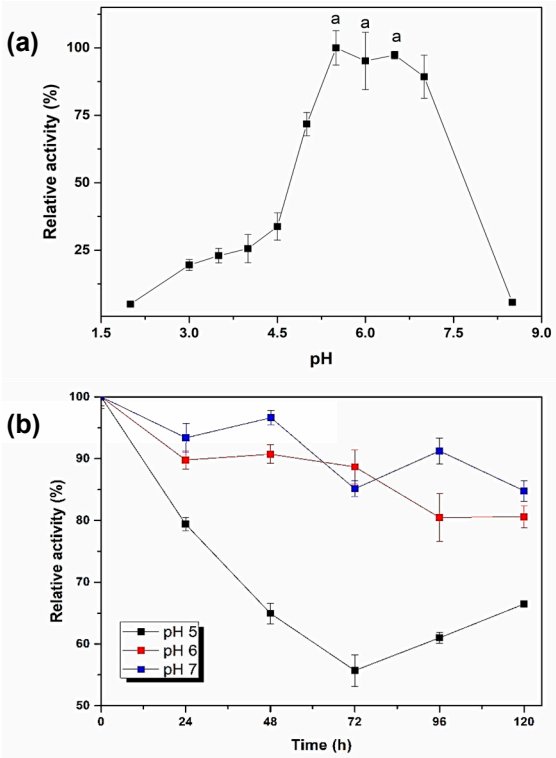


Figure 1. Effect of pH on lysozyme enzymatic activity (**a**) and stability of enzymatic activity over time (**b**).

Lysozyme (type-c from hen egg white) is a small monomeric protein consisting of 129 amino acids, supported by four disulfide linkages that preserve its tertiary structure. Recently, structural studies based on neutron crystallography have indicated that residues near the catalytic site, including Trp108, contribute to the integrity of the active site alongside residues such as Asn44, Asn46, and Asn59, which stabilize the catalytic pair Glu35–Asp52 through an extensive hydrogen-bond network [38]. Furthermore, it is well documented that six tryptophan residues are strategically positioned throughout the protein, enhancing both structural integrity and substrate recognition. Trp62 and Trp108 are situated adjacent to the catalytic cleft and are involved in substrate binding, while Trp28 and Trp111 reside within the hydrophobic core and contribute to stabilizing the tertiary structure [39,40]. Consistent with this structural arrangement, the lysozyme evaluated in this work exhibited significant catalytic activity within the weakly acidic pH range of 5.5–6.5. In slightly acidic circumstances, Glu35 becomes protonated, whereas Asp52 remains negatively charged. This maintains the catalytic conformation needed for effective hydrolysis of β-1,4-glycosidic bonds [9]. The observed decrease in the relative activity at pH 5.5 during the first 48 h may be associated with slight conformational alterations impacting the microenvironment of Trp residues that contribute to structural stabilization, especially those located in the hydrophobic core, without immediately compromising catalytic activity. Additionally, the ability of lysozyme to adapt from slightly acidic to neutral pH was confirmed, which is advantageous for its immobilization in polymeric complexes as, once released, the enzyme could retain its catalytic activity [9,13].

3.2. Physicochemical Characterization of CS–κ-CRG and CS–κ-CRG/Lz Nanoparticles

3.2.1. Particle Size Distribution, ζ-Potential, and Polydispersity Index

The CS–κ-CRG and CS–κ-CRG/Lz nanoparticles obtained exhibited a monomodal distribution with average sizes of 503.3 ± 9.2 and 332.94 ± 5.6 nm, respectively (Figure 2). These values correspond to the hydrodynamic diameter obtained via dynamic light scat-

tering (DLS), which reflects the particle size in suspension including the solvation layer and possible polymer interactions in the medium. The ζ-potential values were positive and did not significantly differ ($p > 0.05$) between CS–κ-CRG and CS–κ-CRG/Lz nanoparticles, with the acidic pH for both nanoparticles and the positive ζ-potential indicating the presence of protonated amino groups on the surface of the nanoparticles. Regarding the polydispersity index (PI), all samples exhibited PDI values lower than 0.3, which agree with a unimodal curve and monodisperse particles distribution ($p < 0.5$) (Table 1). It is important to note that DLS measurements are highly sensitive to particle aggregation and provide intensity-weighted size distributions.

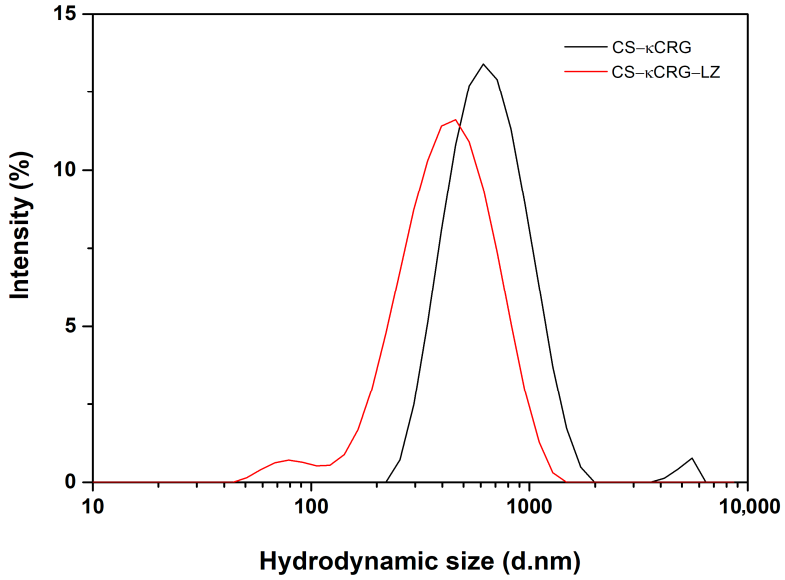


Figure 2. Monomodal distribution of the hydrodynamic diameter of CS–κ-CRG/Lz and CS–κ-CRG nanoparticles.

Table 1. CS–κ-CRG and CS–κ-CRG/Lz nanoparticles: size, ζ-potential, and polydispersity index.

	CS–κ-CRG	CS–κ-CRG/Lz
pH final	5.6 ± 0.01	5.7 ± 0.01
PDI ± S.D.	0.378 ± 0.045	0.243 ± 0.0
Dh ± S.D. [b] (nm)	503.28 ± 9.2 [aC]	332.94 ± 5.6 [bB]
Potential ζ [c] (mV)	+26 ± 6.4 [aA]	+26 ± 1.1 [aA]

Values presented as mean ± S.D. indicate the replicates of three experiments. Tukey's test indicates that values with different letters are significantly different ($p \leq 0.05$).

Recently, Emolaga et al. [35] reported the optimization of CS–κ-CRG nanoparticle formulations using different crosslinking strategies. Their optimized system produced CS–κ-CRG nanoparticles with hydrodynamic diameters of approximately 350 nm. In the present study, slightly larger particle sizes were obtained for the CS–κ-CRG nanoparticles (~503 nm). This difference may be attributed to the absence of additional crosslinking agents in our formulation, since nanoparticle formation relied solely on the electrostatic complexation between positively charged chitosan and negatively charged κ-carrageenan. The lack of external crosslinkers may lead to less compact polyelectrolyte complexes and, consequently, larger hydrodynamic diameters. Hernández-Téllez et al. [19] previously documented the immobilization of lysozyme on chitosan–κ-carrageenan nanoparticles, reporting particle sizes and ζ-potential values similar to those obtained in the present study. A decrease in particle size was observed after the incorporation of lysozyme, resulting in the creation of CS–κ-CRG/Lz nanoparticles, consistent with their findings. This reduction

may be associated with structural rearrangements within the polyelectrolyte complex upon lysozyme incorporation, which can promote additional intermolecular interactions and result in a more compact nanoparticle architecture. The nanoparticle synthesis method may also influence the observed size differences, as lysozyme was first mixed with chitosan prior to the dropwise addition of κ-carrageenan to induce polyelectrolyte complex formation. This sequence may facilitate the formation of chitosan–lysozyme pre-associations that influence the nucleation and assembly of complexes upon the introduction of κ-carrageenan, thereby promoting the development of more compact nanoparticles with reduced hydrodynamic diameters, as typically observed in polyelectrolyte complex systems where assembly conditions significantly influence nanoparticle structure and stability [37,41]. Moreover, lysozyme has been reported to catalyze the hydrolysis of β-(1→4) glycosidic bonds in partially acetylated chitosan, leading to limited polymer degradation depending on the degree of deacetylation [42]. The degree of deacetylation determined in this study (67.6 ± 2.9%) suggests that the chitosan used may be susceptible to partial enzymatic degradation, which could also contribute to the smaller particle size. Nevertheless, electrostatic interactions between κ-carrageenan and chitosan, together with the macromolecular organization within the nanoparticles, may partially limit lysozyme accessibility to the polymer chains. However, additional analyses are needed to validate this theory.

3.2.2. Morphological Analysis of CS–κ-CRG and CS–κ-CRG/Lz Nanoparticles by AFM and TEM

The AFM and TEM micrographs confirm the formation of CS–κ-CRG and CS–κ-CRG/Lz nanoparticles, showing spherical to semispherical agglomerate nanoparticles for both materials. In addition, the average surface diameter of CS–κ-CRG/Lz nanoparticles was 144 ± 40 nm (Figure 3a). This is smaller than the average hydrodynamic diameter obtained via DLS, which can be attributed to the fact that DLS measures the hydrodynamic size of particles in suspension, including the solvation layer and possible polymer chain interactions in the medium, whereas AFM and TEM measurements correspond to the dry state of the nanoparticles [35,43].

3.2.3. Lysozyme Encapsulation Efficiency and Loading Capacity

The encapsulation efficiency of lysozyme within the CS–*κ*-CRG complex was observed to be 63.14 ± 1.24%, while the loading capacity was 28.57 ± 4.0%. These results indicate the successful entrapment of lysozyme within the polyelectrolyte complex nanoparticles. In this study, a pre-loading method was employed for the CS–*κ*-CRG/Lz nanoparticles, which has been reported to facilitate a homogeneous distribution of the active compounds within the polyelectrolyte complex [37]. Hernández-Téllez et al. [19] previously reported an encapsulation efficiency of approximately 70 ± 1.7% for lysozyme associated with chitosan–carrageenan nanoparticles formulated from a combination of κ- and λ-carrageenan. The minor discrepancies observed with the present study may be attributed to variances in carrageenan composition. Specifically, λ-carrageenan includes three sulfate groups per disaccharide unit, which may enhance electrostatic interactions with the protonated amino groups of chitosan and positively charged residues such as lysine and histidine in lysozyme, potentially enhancing protein entrapment within the polyelectrolyte complex. Similarly, Noreen et al. [27] demonstrated that chitosan–carrageenan nanoparticles can act as effective nanocarriers for bioactive compounds, reporting encapsulation efficiencies above 90% for naproxen depending on formulation conditions. In agreement with these reports, the encapsulation efficiency obtained in the present work suggests an effective association within the CS–κ-CRG nanoparticles. This behavior is consistent with the positive ζ-potential observed in both nanoparticle systems, indicating the predominance of protonated amino groups of chitosan on the particle surface in acidic conditions, which enhances colloidal

stability and promotes the retention of lysozyme within the internal structure of the polyelectrolyte complex. This behavior is characteristic of polyelectrolyte complex nanoparticles formed through electrostatic interactions between oppositely charged biopolymers. Interestingly, the incorporation of lysozyme was also accompanied by a reduction in the hydrodynamic diameter of the nanoparticles, suggesting structural rearrangements within the polymeric network. These findings highlight the strong capacity of CS–κ-CRG polyelectrolyte complex nanoparticles to immobilize bioactive compounds, particularly proteins such as lysozyme [19,27,35–37].

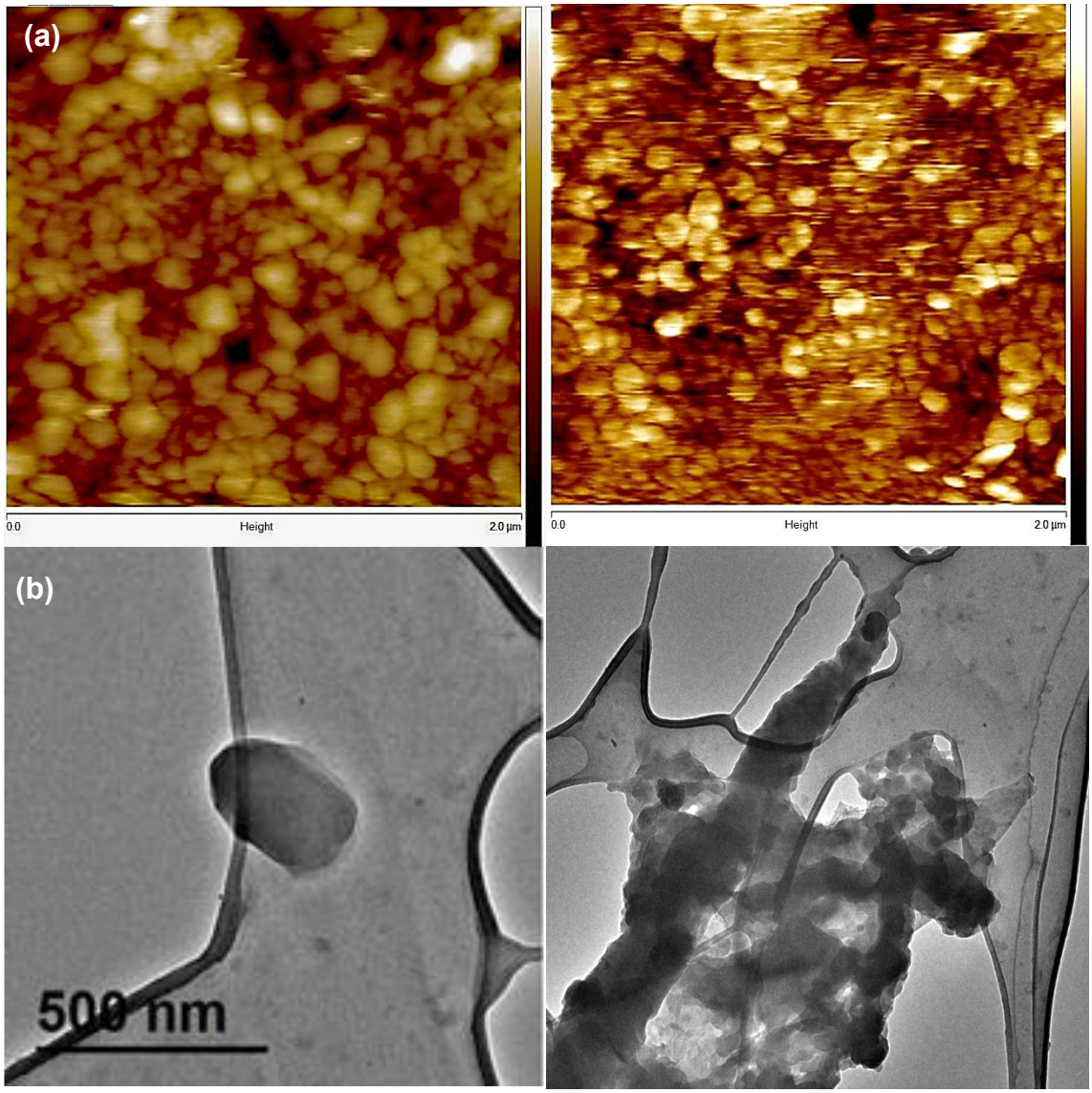


Figure 3. CS–κ-CRG/Lz nanoparticle morphology: (**a**) Atomic force microscopy (AFM) and (**b**) transmission electron microscopy (TEM). Average surface size: 144.4 ± 39.8 nm.

3.2.4. FT-IR Spectroscopy Analysis

FT-IR spectroscopy was performed to identify the functional groups and possible interactions among chitosan, κ-carrageenan, and lysozyme in the CS–κ-CRG/Lz nanoparticle systems (Figure 4). For both CS–κ-CRG and CS–κ-CRG/Lz nanoparticles, a broad absorption band was observed around 3325 and 3230 cm^{-1}, respectively, which corresponds to overlapping O–H and N–H stretching vibrations associated with hydrogen bonding within the polymeric network. The characteristic bands of the amino groups may be partially overlapped by the broad hydroxyl stretching band in this region.

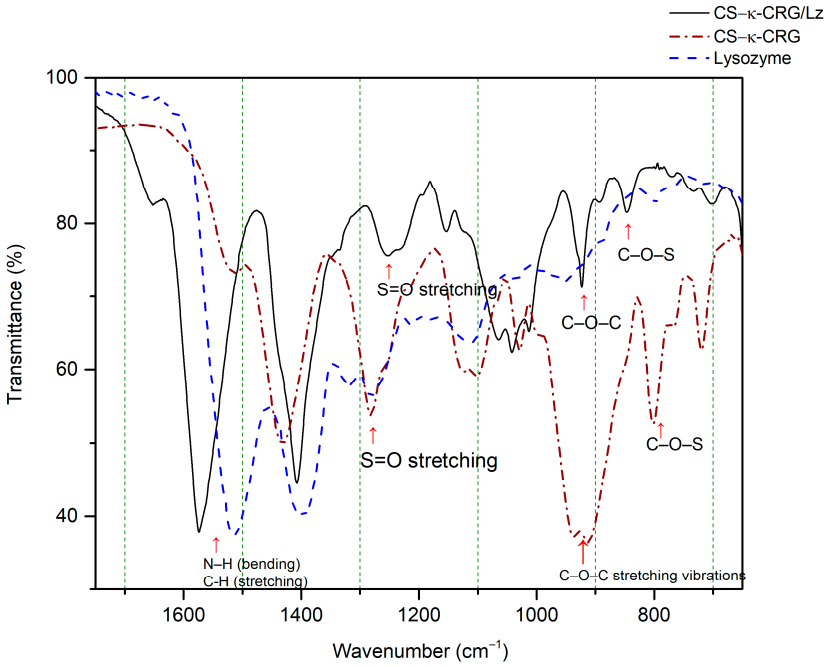


Figure 4. FT-IR spectra of CS–κ-CRG/Lz and CS–κ-CRG nanoparticles. Green dashed lines are included as visual guides to highlight the relevant FTIR bands.

In the spectrum of lysozyme, a characteristic band around 1550 cm^{-1} corresponding to the amide II vibration was observed. This band was also detected in the CS–κ-CRG/Lz nanoparticles, confirming the successful incorporation of lysozyme within the polymeric matrix. Slight variations in the intensity of this band suggest intermolecular interactions between the protein and the polysaccharide components of the polyelectrolyte complex. The absorption peak assigned to the sulfate ester group (S=O stretching) of κ-carrageenan appeared at approximately 1283 cm^{-1} in CS–κ-CRG nanoparticles, while a decrease in intensity and a slight shift toward approximately 1253 cm^{-1} was observed in the CS–κ-CRG/Lz system. These spectral changes suggest electrostatic interactions between the negatively charged sulfate groups of κ-carrageenan and the protonated amino groups of chitosan, which are characteristic of polyelectrolyte complex formation [19,24,35].

Additional bands observed around 908 to 939 cm^{-1} correspond to C–O–C stretching vibrations of the polysaccharide backbone, which are characteristic of the glycosidic linkages present in chitosan and carrageenan [44]. The presence of these bands indicates that the polysaccharide structure is preserved after nanoparticle formation. Furthermore, the band near 840 cm^{-1}, attributed to the C–O–S vibration of sulfate groups in κ-carrageenan, showed slight variations in the CS–κ-CRG/Lz nanoparticles compared with CS–κ-CRG. These changes may indicate modifications in the local environment of sulfate groups due to interactions within the polyelectrolyte complex after lysozyme incorporation [35].

3.3. Antifungal Effects of CS–κ-CRG and CS–κ-CRG/Lz Nanoparticles on Early Development of Colletotrichum siamense

3.3.1. Reduction of Conidial Viability by CS–κ-CRG and CS–κ-CRG/Lz Nanoparticles

The antifungal efficacy of CS–κ-CRG/Lz and CS–κ-CRG nanoparticles, as well as hen egg white lysozyme and the commercial fungicide flutriafol against *C. siamense*, was determined using a conidial viability test. Although lysozyme is mainly recognized for its antibacterial properties, various studies have revealed its antifungal capabilities against clinical filamentous fungi and yeast. Lysozyme may interact with negatively charged fungal cell surfaces, resulting in membrane instability and structural impairment. The enzyme may also influence polysaccharides in the fungal cellular stress responses that

diminish fungal viability [11,45], particularly by disrupting the synthesis of essential cell wall components, which further contributes to the antifungal effects of lysozyme. The enzymatic degradation of cell wall components is presumed to be a crucial antifungal mechanism for hydrolytic enzymes, thereby underscoring the potential role of lysozyme in undermining fungal cell integrity [9,46]. However, scientific evidence for the activity of lysozyme against phytopathogenic fungi such as *Colletotrichum* spp. remains limited. In this study, lysozyme and flutriafol exhibited a low capacity to decrease the viability of *C. siamense* conidia, yielding viability percentages over 75%, comparable to the untreated control across all assessed concentrations ($p > 0.05$). This finding suggests that elevated doses of lysozyme and flutriafol are necessary to diminish the viability of *C. siamense* conidia, despite prior evidence demonstrating that *C. fructicola* and *C. siamense* exhibited significant susceptibility to flutriafol, while *C. truncatum* and *C. nymphaeae* showed diminished sensitivity or resistance, with EC_{50} values surpassing 50 $\mu g \cdot mL^{-1}$ [47].

Treatment with CS–κ-CRG nanoparticles at concentrations ranging from 90 to 300 $\mu g \cdot mL^{-1}$ markedly decreased the viability of *C. siamense* conidia, resulting in viability percentages between 64.3 and 45.7%, compared to the untreated control (>95%) ($p = 3.61109 \times 10^{-7}$). The CS–κ-CRG/Lz nanoparticles also reduced the viability, showing percentages between 54.9 and 51.5 % relative to the untreated control. Although the CS–κ-CRG nanoparticles exhibited higher conidial viability inhibition percentages compared to the CS–κ-CRG/Lz nanoparticles, no significant differences were observed between the two treatments at the tested dosages at 8 h incubation ($p = 0.728$) (Figure 5a). After 12 h of incubation, the inhibitory effect remained evident. At the maximum dose of 300 $\mu g \cdot mL^{-1}$, the viability of the conidia consistently decreased compared to the untreated control ($p = 7.12327 \times 10^{-4}$); here, the viability percentages decreased to 53% for CS–κ-CRG/Lz nanoparticles and 47% for CS–κ-CRG nanoparticles.

The sustained reduction in conidial viability observed for both nanoparticle systems is consistent with the antifungal behavior previously described for chitosan-based nanomaterials, primarily due to the presence of protonated amino groups that allow electrostatic interactions with negatively charged components of the fungal cell surface, as well as the nanometric size of CS nanoparticles, which may increase the interaction area with the fungal surface. These interactions may alter cell wall organization and compromise membrane integrity, increase permeability, and ultimately impair cellular metabolism and viability [48,49].

The reduced initial activity observed for CS–κ-CRG/Lz nanoparticles compared to CS–κ-CRG nanoparticles may be attributed to the characteristics of the polymeric matrix; for example, resulting from a reduced amount of amino groups in CS due to intermolecular interactions within the nanoparticle system. In addition, previous studies have demonstrated that chitosan-based nanostructures might influence the availability or release kinetics of encapsulated biomolecules, potentially delaying their biological effects based on the duration of exposure. Lysozyme encapsulated in chitosan-based nanoparticles demonstrates sustained release profiles, with the enzyme gradually released from the polymer network due to electrostatic interactions and matrix-stabilizing effects [14]. Moreover, encapsulated chitinase systems have demonstrated improved antifungal efficacy and stability against *Colletotrichum* spp., indicating that polymeric or nanostructured matrices may protect the enzyme and facilitate controlled release of the active catalyst [15]. This controlled release behavior might delay lysozyme activity, which could explain the decreased conidial viability observed after longer exposure times compared with 8 h of incubation; however, further studies are needed for the CS–κ-CRG/Lz nanoparticles. The median inhibitory concentrations (IC_{50}) of CS–κ-CRG and CS–κ-CRG/Lz nanoparticles were determined at 8 and 12 h of incubation, respectively, according to the viability percentage data. The concentrations for

CS–κ-CRG nanoparticles were 175 ± 11 and 278 ± 25 μg·mL^{-1}; while, for CS–κ-CRG/Lz nanoparticles, they were 338 ± 80 and 420 ± 95 μg·mL^{-1}, respectively. The determined IC_{50} values were utilized to select appropriate concentrations for subsequent tests.

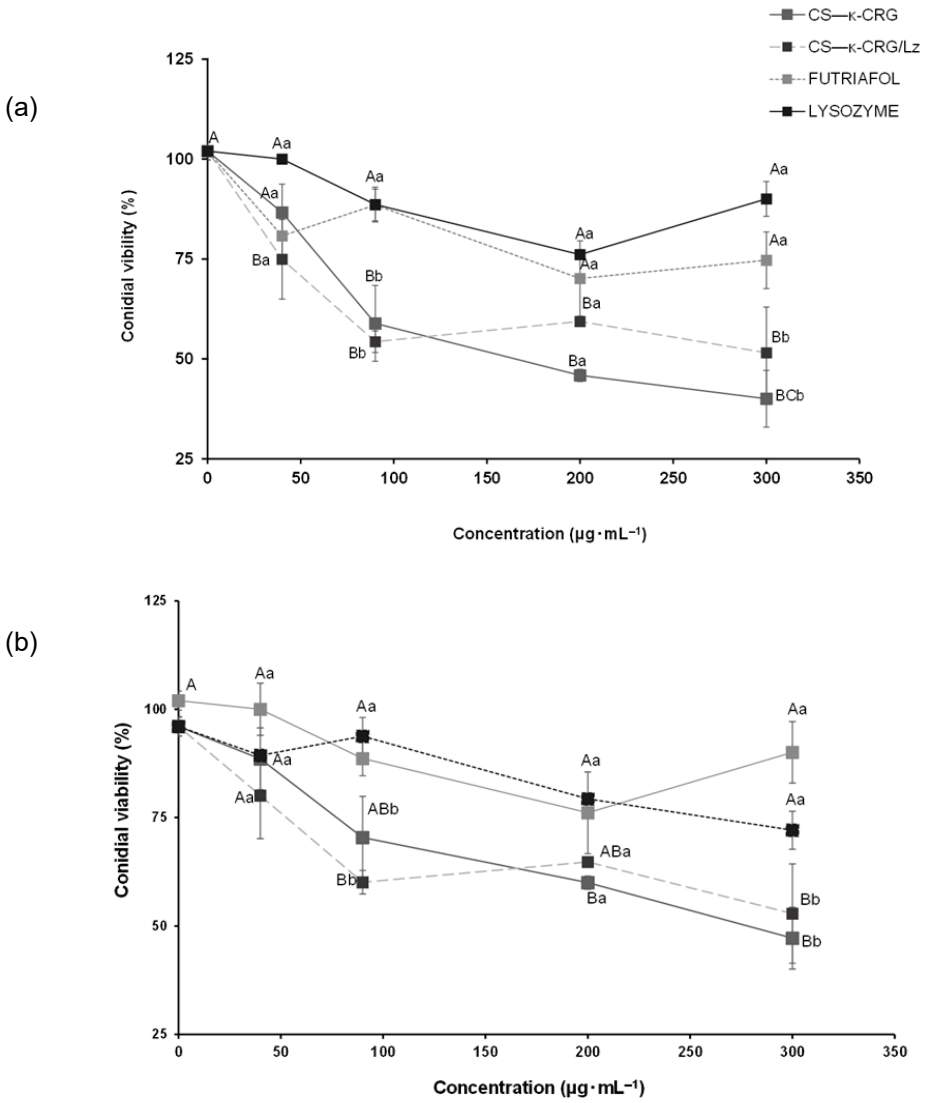


Figure 5. Fungistatic effect of CS–κ-CRG/Lz and CS–κ-CRG nanoparticles on conidial viability of *Colletotrichum siamense*: (**a**) 8 h of incubation and (**b**) 12 h of incubation. Different letters indicate statistically significant differences among treatments ($p < 0.05$).

3.3.2. Delay of Conidial Germination and Changes in Germination Kinetics

The percentage of conidia that germinated over a 24 h period was monitored to determine the degree of damage caused by the CS–κ-CRG and CS–κ-CRG/Lz nanoparticles during the conidia growth phase (early growth stage). When the CS–κ-CRG and CS–κ-CRG/Lz nanoparticles were used at a concentration of 330 μg·mL^{-1}, the germination process was noticeably reduced to 14% and 2%, respectively, compared to the control (pH 7) ($p \leq 0.05$) for up to 6 h (Figure 6). In the same way, a delay of up to 6 h was observed with the CS–κ-CRG and CS–κ-CRG/Lz nanoparticles at a concentration of 200 μg·mL^{-1} ($p \leq 0.05$); however, the germination rates were higher, reaching 52 and 57%, respectively. After 12 h, the germination process of fungi after exposure to CS–κ-CRG and CS–κ-CRG/Lz nanoparticles at a concentration of 330 μg·mL^{-1} achieved percentages of 60 and 62%, respectively. At a concentration of 200 μg·mL^{-1}, uncontrolled germination was noted, with percentages surpassing 80%, significantly greater than the control ($p \leq 0.05$). At 18 h,

only the 330 μg·mL^{-1} concentration of CS–κ-CRG nanoparticles exhibited a germination percentage lower than that of the other treatments; nonetheless, 100% germination was achieved by 24 h.

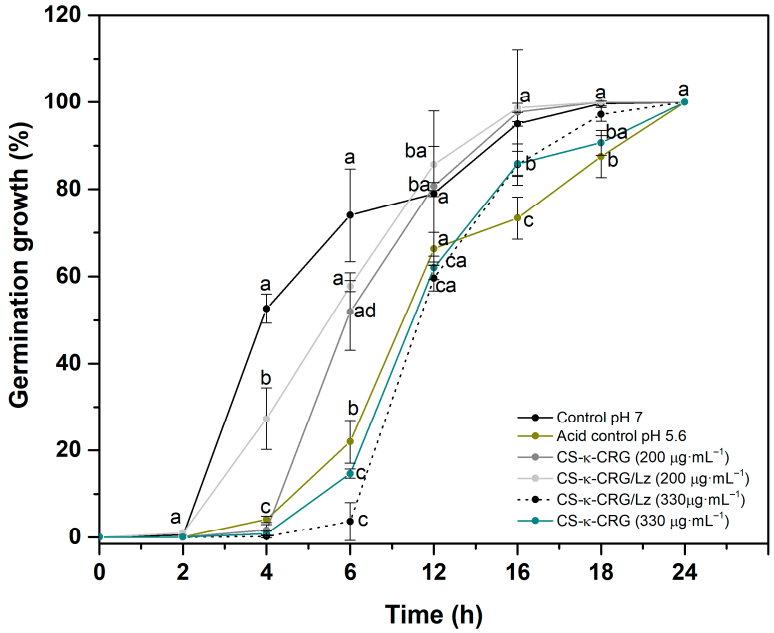


Figure 6. Delay effect on the germination process of *C. siamense* exposed to CS–κ-CRG/Lz and CS–κ-CRG nanoparticles. Different letters indicate statistically significant differences among treatments ($p < 0.05$).

A decrease of about 30% in conidial germination was observed after 18 h in the acidic control at pH 5.6 (acetic acid), compared to the control at pH 7 (100% of germination) ($p \leq 0.05$). Table 2 shows the kinetic germination parameters estimated by fitting the experimental data of germination percentages of *C. siamense* to a logistic model. The germination rate k (h^{-1}) indicates that both CS–*κ*-CRG and CS–*κ*-CRG/Lz nanoparticles at 330 μg·mL^{-1} can delay the germination process for up to 12 h, compared to the control (Figure 6).

Table 2. Kinetic parameters of *Colletotrichum siamense* exposed to CS–*κ*-CRG and CS–*κ*-CRG/Lz nanoparticles.

Kinetic Parameters	Control		CS–*κ*-CRG		CS–*κ*-CRG/Lz	
	pH 7	pH 5.6	200 μg·mL^{-1}	300 μg·mL^{-1}	200 μg·mL^{-1}	300 μg·mL^{-1}
S_{max} (%)	90.3 ± 2.82	82.8 ± 3.06	92.8 ± 2.41	93.2 ± 1.91	94.9 ± 1.97	95.7 ± 2.15
S_0 (%)	0.38 ± 0.58	1.46 ± 0.61	0.001 ± 0.003	0.86 ± 0.24	1.43 ± 0.72	0.17 ±0.13
k (h^{-1})	1.42 ± 0.38	0.45 ± 0.06	2.11 ± 1.24	0.45 ± 0.03	0.78 ± 0.098	0.56 ± 0.06
R^2	0.981	0.989	0.988	0.997	0.991	0.997

To date, limited studies have been published on the control of *C. siamense* using antimicrobial enzymes loaded in CS nanoparticles. Table 2 and Figure 6 indicate that the CS–*κ*-CRG/Lz and CS–*κ*-CRG nanoparticles can delay the germination process. The lag phase during the germination process of filamentous fungi under optimal growth conditions represents the time needed to adapt to the physical and chemical environment. In this context, compared to the controls (pH 7 and 5.6), both types of nanoparticles (CS–*κ*-CRG and CS–*κ*-CRG/Lz) showed a moderate effect on maximum conidial germination (S_{max}), which could be attributed to a possible physiological and metabolic adaptation of *C. siamense* to CS nanomaterials exposure. López-Bermudez et al. [8] reported a low

bioactivity of large CS nanoparticles (582.2 ± 3.5 nm) at 1 mg·mL^{-1} against *C. fructicola* isolates on radial growth. Similar behavior was found by Hernández-López et al. [18], who reported that CS nanoparticles at 1 mg·mL^{-1} with 300 nm reduced *C. siamense* conidial germination by 16% until 6 h, although 100% of germination was achieved after 10 h. Together, these studies suggest a relatively low initial sensitivity of *Colletotrichum* spp. to chitosan nanomaterials. This behavior may be related to fungal adaptive mechanisms, as filamentous fungi can remodel their cell wall through the production of enzymes such as chitinases, glucanases, and chitin deacetylases, which modify chitin-derived polymers and contribute to reduced susceptibility to chitosan-based materials [21,50].

Although a comparable pattern was observed with the CS–κ-CRG/Lz and CS–κ-CRG nanoparticle systems, the inhibition of conidial germination was prolonged to 16 h. Even though the average particle sizes in this study are similar to those reported in previous studies (based on DLS analysis), the CS–κ-CRG/Lz and CS–κ-CRG nanoparticle systems exhibited antifungal activity at considerably lower doses. This improved activity may be associated with the polyelectrolyte matrix formed between chitosan and κ-carrageenan, which can enhance nanoparticle stability and promote a more sustained interaction with the fungal surface.

3.3.3. Morphometric Alterations During Conidial Germination and Hyphal Development

The exposure of *C. siamense* conidia to CS–κ-CRG and CS–κ-CRG/Lz nanoparticles caused changes in the shape and size of the conidia, hyphae, and appressoria formation during the germination stage (Table 3, Figure 7). Natural swelling of conidia during germination was observed in control media at 2 h post-inoculation, consistent with the typical fungal development of *Colletotrichum* spp. (Figure 7a–d). The final average dimensions (width × length) of the germinated conidia were 6.82 ± 1.45 × 14.93 ± 2.25 µm, with hyphal width of 3.35 ± 0.59 µm and appressoria diameter of 7.04 ± 0.86 µm. The morphometric analysis showed that CS–κ-CRG/Lz nanoparticles at 200 µg·mL^{-1} significantly increased the conidia width and length at all evaluated times; similar effects were observed at 330 µg·mL^{-1} ($p < 0.05$). Additionally, the hyphal width and the appressoria diameter showed significant size increments with respect to the control ($p < 0.05$) (Table 3). Structural changes and deformations characterized by disorganized conidia with amorphous shapes, hyphal distortion and segmentation, and many small vacuoles inside, were observed (Figure 7i–l). Similar changes were induced by the CS–κ-CRG nanoparticles, with increased conidial width and length, hyphal width, and appressorial diameter at 200 and 330 µg·mL^{-1}, leading to notable changes observed at 12 h of germination ($p < 0.05$) (Table 3). Figure 7e–h show disorganized conidia with amorphous shapes, hyphal distortion, and segmentation, as well as many large vacuoles inside compared to those treated with CS–κ-CRG/Lz nanoparticles.

The dynamic capacity of cell walls and the selectivity of the plasma membrane are critical for fungal growth and nourishment, allowing water and essential nutrients to pass through undisturbed [51]. The results of the present work confirm that chitosan-based materials are associated with damage to fungal plasma membranes and disruption of cell wall organization [18,49,50]. Bright-field analysis and morphometric measures were used to investigate the effects of chitosan nanoparticles on the morphology of *Colletotrichum siamense*. The observations revealed amorphous conidia and hyphal structures, abundant vesicle-like structures, protrusions at atypical cellular locations, and both lateral and apical branching (Figure 7).

Table 3. Influence of CS–*κ*-CRG and CS–*κ*-CRG/Lz nanoparticles on the morphometric attributes of *Colletotrichum siamense*.

CS–*κ*-CRG Nanoparticles					
Time (h)	**Concentration (μg·mL^{-1})**	**Conidia**		**Hyphal**	**Appressoria**
		Width (μm)	**Length (μm)**	**Width (μm)**	**Diameter (μm)**
0	200	5.75 ± 0.55	13.81 ± 1.36	ND	ND
2		6.29 ± 0.51 ^{Ab}	14.24 ± 1.12 ^{a}	ND	ND
4		6.60 ± 0.58 ^{Ab}	15 ± 1.49 ^{b}	ND	ND
6		6.69 ± 0.73 ^{ABb}	14.97 ± 1.87 ^{a}	ND	ND
12		6.84 ± 0.77 ^{ABb}	15.04 ± 2.17 ^{a}	3.67 ± 0.51 ^{c}	7.32 ± 0.68 ^{a}
16		7.14 ± 0.81 ^{Bb}	17.15 ± 3.25 ^{b}	4.07 ± 0.62 ^{b}	7.49 ± 0.78 ^{a}
18		7.16 ± 0.94 ^{Ba}	15.41 ± 2.80 ^{a}	4.07 ± 0.54 ^{b}	7.45 ± 0.58 ^{b}
0	330	5.75 ± 0.55	13.81 ± 1.36	ND	ND
2		5.84 ± 0.64 ^{Aca}	13.84 ± 1.41 ^{a}	ND	ND
4		5.99 ± 0.72 ^{Ac}	14.57 ± 1.71 ^{b}	ND	ND
6		6.33 ± 0.91 ^{Aba}	14.82 ± 1.99 ^{a}	ND	ND
12		6.47 ± 1.10 ^{Bb}	15.25 ± 1.31 ^{a}	3.41 ± 0.36 ^{b}	7.13 ± 0.94 ^{a}
16		6.83 ± 1.00 ^{Bb}	14.89 ± 1.49 ^{c}	3.48 ± 0.67 ^{b}	7.30 ± 0.81 ^{a}
18		6.50 ± 1.60 ^{Ba}	15.11 ± 2.38 ^{a}	3.53 ± 0.56 ^{a}	8.80 ± 1.40 ^{c}
CS–*κ*-CRG/Lz nanoparticles					
Time (h)	Concentration (μg·mL^{-1})	Conidia		Hyphal	Appressoria
		Width (μm)	Length (μm)	Width (μm)	Diameter (μm)
0	200	5.75 ± 0.55	13.81 ± 1.36	ND	ND
2		6.35 ± 0.45 ^{Ad}	14.40 ± 1.13 ^{a}	ND	ND
4		6.39 ± 0.60 ^{Ab}	13.99 ± 1.51 ^{ac}	ND	ND
6		6.59 ± 0.72 ^{Aa}	14.58 ± 1.48 ^{a}	ND	ND
12		6.63 ± 0.73 ^{Acb}	15.55 ± 2.13 ^{a}	3.68 ± 0.55 ^{c}	6.81 ± 0.56 ^{b}
16		6.67 ± 0.73 ^{Ab}	15.43 ± 2.26 ^{c}	3.76 ± 0.44 ^{b}	6.95 ± 0.48 ^{a}
18		7.14 ± 0.83 ^{Ba}	15.11 ± 1.82 ^{a}	4.04 ± 0.45 ^{b}	7.00 ± 1.17 ^{a}
0	330	5.75 ± 0.55	13.81 ± 1.36	ND	ND
2		6.07 ± 0.79 ^{Aa}	13.90 ± 1.38 ^{a}	ND	ND
4		5.91 ± 0.66 ^{Adc}	14.05 ± 1.78 ^{ac}	ND	ND
6		6.29 ± 0.80 ^{Aba}	14.89 ± 2.00 ^{a}	ND	ND
12		6.65 ± 0.59 ^{Bc}	14.65 ± 1.5 ^{a}	3.46 ± 0.46 ^{c}	7.65 ± 0.96 ^{a}
16		7.01 ± 0.96 ^{Bcb}	14.74 ± 2.52 ^{c}	3.56 ± 0.47 ^{b}	8.96 ± 1.33 ^{b}
18		7.08 ± 1.00 ^{Ba}	14.95 ± 2.64 ^{a}	3.38 ± 0.61 ^{a}	8.05 ± 0.97 ^{c}
Control (pH 5.6)					
Time (h)	Concentration (μg·mL^{-1})	Conidia		Hyphal	Appressoria
		Width (μm)	Length (μm)	Width (μm)	Diameter (μm)
0	0	5.75 ± 0.55 ^{A}	13.81 ± 1.36 ^{a}	ND	ND
2		5.85 ± 0.59 ^{Aa}	14.37 ± 1.62 ^{a}	ND	ND
4		5.87 ± 0.68 ^{Aa}	14.12 ± 1.42 ^{a}	ND	ND
6		6.26 ± 0.85 ^{Aa}	14.58 ± 1.67 ^{a}	ND	ND
12		6.18 ± 0.7 ^{Aa}	13.75 ± 2.12 ^{a}	2.93 ± 0.38 ^{a}	7.67 ± 0.73 ^{a}
16		6.12 ± 0.55 ^{Aa}	13.89 ± 1.06 ^{a}	2.83 ± 0.43 ^{a}	7.49 ± 0.71 ^{a}
18		6.82 ± 1.45 ^{Ba}	14.93 ± 2.25 ^{a}	3.35 ± 0.59 ^{a}	7.04 ±0.86 ^{a}

The conidia width and length, average of 60 measurements ± SD. Hyphae and appressoria diameters, average of 60 measurements ± SD. Uppercase letters indicate significant differences between treatment durations ($p < 0.05$) using Tukey's multiple range test. Lowercase letters indicate significant differences between treatments at the same time ($p < 0.05$) using Tukey's multiple range test. ND: not determined.

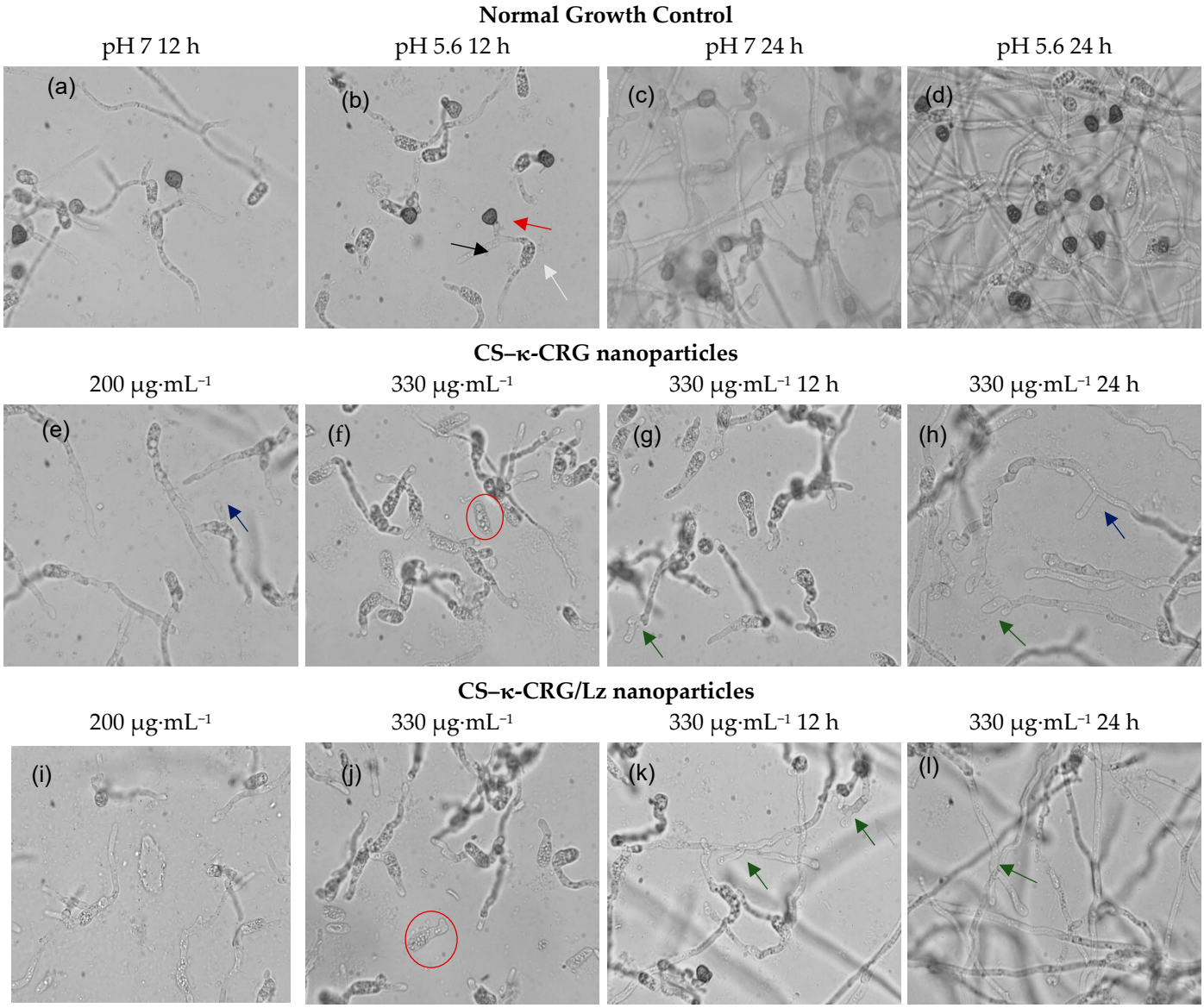


Figure 7. Morphological alterations in C. siamense conidial germination caused by CS–κ-CRG and CS–κ-CRG/Lz nanoparticles. (**a**–**d**) Germination growth under optimum conditions, (→) black: Primary hypha, (→) white: polarized germinated conidia, (→) red: appressorium structure; (**e**–**h**) Morphological abnormalities induced by CS–κ-CRG nanoparticles, red circle: hypervacuolization, (→) blue: lateral branching, (→) green: apical branching; (**i**–**l**) Morphological abnormalities induced by CS–κ-CRG/Lz nanoparticles, red circle: hypervacuolization, (→) green: apical branching.

Under normal growth conditions, conidia of filamentous fungi germinate through a series of morphological events, including conidial swelling (rehydration), cytoskeletal reorganization, and the establishment of polarized growth. This polarization leads to the emergence of a primary germ tube from the conidium. The germ tube then elongates through apical growth, giving rise to primary hyphae. During subsequent vegetative growth, new polarity axes develop along the hyphae, leading to lateral branching [51,52]. Hyphal branching is a crucial cellular event for phytopathogenic fungi, as it enhances effective host colonization and mycelial development. Harris et al. [52,53] suggested that hyphal branching patterns are influenced by environmental conditions, which can cause both apical and lateral branching. Notably, apical branching has been described as an emergency growth response under stressful conditions, potentially resulting in damage or

interference with vesicle transport mechanisms to the main apex, disruptions in cytoplasmic organization, or mutations.

3.3.4. Concentration-Dependent Modulation of Appressorium Development

Figure 8 shows an unexpected and significant reduction ($p < 0.05$) in the formation of appressoria in *C. siamense* conidia exposed to CS–κ-CRG and CS–κ-CRG/Lz nanoparticles with respect to the acidified control. The CS–κ-CRG nanoparticles at concentrations of 330 and 200 μg·mL^{-1} significantly inhibited appressoria formation at 12, 18, and 24 h compared to the control, which was more than 85% less ($p < 0.05$). The CS–κ-CRG/Lz nanoparticles at 330 and 200 μg·mL^{-1} reduced the amount of appressoria formed at all time points examined, with a stronger effect at the 200 μg·mL^{-1} concentration.

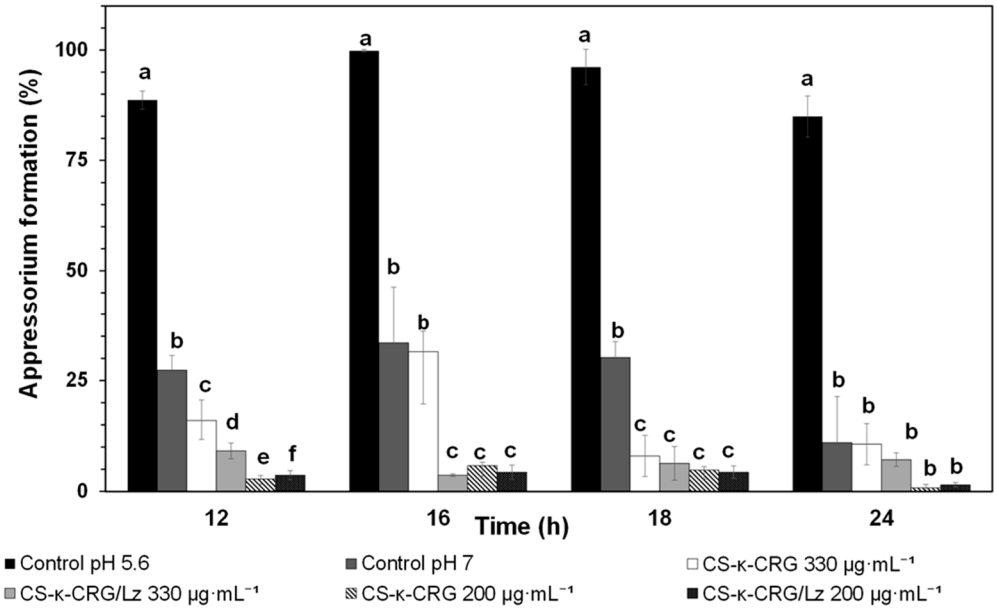


Figure 8. Effects of CS–κ-CRG and CS–κ-CRG/Lz nanoparticles on appressorium formation in *Colletotrichum siamense.* Lowercase letters indicate significant differences between treatments at the same time ($p < 0.05$) using Tukey's multiple range test.

Appressorium formation is a key step in the infection process of *Colletotrichum* species, as these specialized structures generate the mechanical force required for host penetration through a narrow penetration peg emerging from the appressorium base [5]. Currently, there are limited reports linking chitosan or its nanomaterials to their potential role as modulators or inhibitors of appressorium formation and penetration. However, Lopez-Moya et al. [21] provided evidence that a chitosan solution (LMW) at 5 mg·mL^{-1} can block the appressorium-mediated plant infection of *Magnaporthe oryzae* on rice, affecting appressorium differentiation and resulting in an amorphous shape and reduced size. These findings align with the morphometric analysis and appressoria formation of *C. siamense* growth after exposure to CS–κ-CRG and CS–κ-CRG/Lz nanoparticles in this study, indicating that chitosan nanomaterials may mitigate the pathogenicity-related processes of *Colletotrichum*.

Despite an overall decrease in appressorium formation relative to the acidified control (pH 5.6), treatment with 200 μg·mL^{-1} of the CS–κ-CRG nanoparticles led to a significant enhancement ($p < 0.05$) in the development of these pathogenicity-related structures compared to the CS–κ-CRG/Lz nanoparticles at 16 h (Figure 8).

The increased appressorium formation noted at 200 μg·mL^{-1} concentration of CS–κ-CRG nanoparticles indicates a stress-mediated morphogenetic response. In filamentous

phytopathogenic fungi, sublethal stress can trigger adaptive developmental processes, including the formation of infection structures such as appressoria that help the fungus to penetrate the host [54]. Cellular stress-related processes, especially autophagy pathways such as mitophagy, have been demonstrated to govern fungal development and morphogenesis associated with infection [4,55]. Additionally, the stimulation of appressorium formation may reflect a hormetic response to sublethal nanoparticle stress. Hormesis is a biphasic response, with low concentrations stimulating growth or virulence, whereas higher concentrations exert inhibitory effects [56]. This behavior has been reported for several fungicides, including carbendazim and dimethachlone, which increase mycelial growth or virulence at sublethal doses in phytopathogenic fungi [57,58]. These findings are important in order to avoid using chitosan-based nanomaterials at sublethal doses, which could increase infection-related responses instead of stopping fungal pathogenicity, and identifying optimal concentrations for field application.

3.3.5. Fluorescence-Based Evidence of Cell Wall and Membrane Integrity Disruption

Staining with calcofluor white (CW) and propidium iodide (PI) revealed that the CS–κ-CRG/Lz and CS–κ-CRG nanoparticles affected the structural integrity of the outer cellular barriers of *Colletotrichum siamense*. In cells exposed to CS–κ-CRG nanoparticles at 200 and 330 $\mu g \cdot mL^{-1}$ (Figure 9e,h), CW staining showed a markedly lower fluorescence intensity compared with the control, suggesting alterations in cell wall organization and in the distribution of chitin- and glucan-containing polymers. Conidia treated with CS–κ-CRG/Lz nanoparticles at 200 and 330 $\mu g \cdot mL^{-1}$ exhibited an irregular CW staining pattern (Figure 9k,n), in which the cell wall was poorly defined compared with the well-organized structures observed in the control. Interestingly, localized CW fluorescence was detected mainly at hyphal tips, frequently overlapping with PI staining, suggesting that the apical regions of hyphae may be particularly susceptible to nanoparticle-induced damage affecting both membrane stability and cell wall assembly. Furthermore, PI staining clearly penetrated germinated conidia and hyphae treated with the CS–κ-CRG/Lz and CS–κ-CRG nanoparticles at 200 and 330 $\mu g \cdot mL^{-1}$ (Figure 9f,i,l,o), suggesting compromised plasma membrane integrity. Similar membrane-permeabilizing effects in several filamentous fungi exposed to chitosan-based nanomaterials have been documented, suggesting that the electrostatic interactions between positively charged amino groups of chitosan and negatively charged membrane components, particularly phospholipids, mainly lead to membrane permeabilization, oxidative stress, and disruption of cytoskeletal organization [21,50,59]. These disturbances affect vesicle trafficking and polarized growth, processes that are essential for hyphal elongation and differentiation of infection structures, which could enhance fungal susceptibility to external stresses, including fungicides.

Well-defined germinated conidia, hyphae, and appressoria were observed on the control micrographs, with continuous CW staining and no evidence of membrane permeability, indicating normal cellular development (Figure 9a–c). In contrast, the observations reported in this study are supported by the bright-field micrographs, morphometric analysis, and appressorium formation, which revealed abnormal morphologies including irregular or amorphous hyphal growth, protrusions along the hyphae, and deformed or elongated conidia.

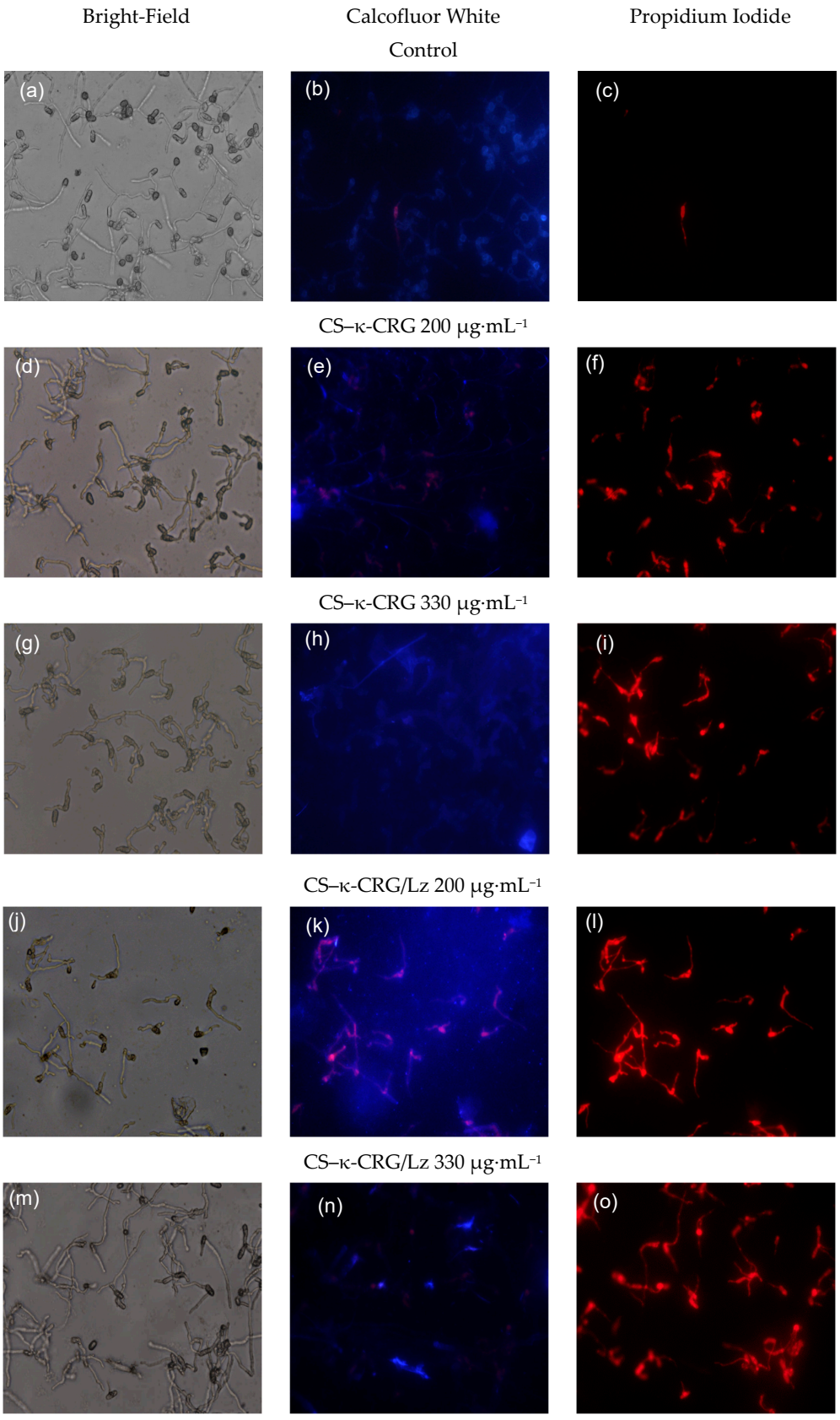


Figure 9. Morphological effects of CS–κ-CRG and CS–κ-CRG/Lz nanoparticles on the cell membrane and cell wall of *Colletotrichum siamense*: (**a**,**d**,**g**,**j**,**m**) Bright-field microscopy images at 40× magnification; (**b**,**e**,**h**,**k**,**n**) Calcofluor white staining at 40×; (**c**,**f**,**i**,**l**,**o**) Propidium iodide staining at 40×.

Numerous studies have demonstrated that phytopathogenic filamentous fungi have developed resistance mechanisms to standard fungicides, including triazole fungicides like flutriafol, which predominantly inhibit the sterol 14 α-demethylase enzyme (CYP51) in the ergosterol production pathway, changing fungal membrane composition and impairing growth [60,61]. In contrast, the current study demonstrates that chitosan-based nanoparticles influence fungal cells via multiple physicochemical interactions, which may explain the abnormal hyphal morphogenesis and the reduced formation of appressoria observed in the treated samples, supporting the idea that chitosan-based nanomaterials interfere with key processes required for fungal growth and pathogenic development.

4. Conclusions

This research demonstrates that CS–κ-CRG and CS–κ-CRG/Lz nanoparticles inhibit *Colletotrichum siamense* during essential early stages of infection, including conidial viability, germination, hyphal growth, and appressorium development. Both formulations induced marked morphological alterations associated with disruption of membrane integrity and cell wall organization. Although the incorporation of lysozyme increased structural damage, it did not confer clear fungistatic superiority over CS–κ-CRG, suggesting that its activity may be partially limited by interactions within the polyelectrolyte matrix.

The antifungal response was concentration-dependent: higher concentrations consistently inhibited appressorium development, whereas an intermediate concentration of CS–κ-CRG stimulated appressorium formation, suggesting a stress-induced morphogenetic response. These findings highlight both the potential and the complexity of chitosan-based nanomaterials for controlling phytopathogenic fungi and underscore the importance of mechanistic and dose–response studies before field application.

Author Contributions: A.C.G.-I.: Conceptualization, Methodology Formal analysis, Investigation, Visualization, Supervision, Writing—Original Draft, Writing—Review and Editing. I.I.H.-V.: Formal analysis, Investigation. W.M.A.-M.: Resources, Supervision, Writing—Review and Editing. A.d.J.R.-D.: Methodology, Formal analysis. A.B.-H.: Methodology, Formal analysis. A.K.L.-M.: Methodology, Formal analysis. M.P.-J.: Conceptualization, Resources, Supervision, Writing—Review and Editing, Funding acquisition. All authors have read and agreed to the published version of the manuscript.

Funding: This project was funded by SECIHTI previously CONAHCyT (grant number 219786) and Universidad de Sonora internal project No. USO313009548. Part of this study was funded by the Mexican Secretariat of Science, Humanities, Technology and Innovation (SECIHTI) through the postdoctoral research project "Phytotoxicity, shelf life and quality parameters in fruits with food-grade biopolymeric coatings for the control of *Alternaria* sp. and *Colletotrichum* sp.", approved in the 2022 Call "Estancias postdoctorales por Mexico".

Data Availability Statement: The data presented in this study are available from the corresponding author upon reasonable request.

Acknowledgments: Gratitude is extended to the Microbiology and Mycotoxins Laboratory from the Department of Research and Postgraduate Studies in Food at the University of Sonora. The morphological analyses of the nanomaterials were performed in collaboration with the Polymer and Materials Research Department at the University of Sonora, which has a JEM 2010F Transmission Electron Microscope available for use.

Conflicts of Interest: The authors declare no conflicts of interest.

Abbreviations

CS–κ-CRG	Chitosan–kappa-carrageenan
CS–κ-CRG/Lz	Chitosan–kappa-carrageenan/lysozyme
PDI	polydispersity index
Dh	hydrodynamic diameter

References

1. Tsushima, A.; Shirasu, K. Genomic Resources of *Colletotrichum* Fungi: Development and Application. *J. Gen. Plant Pathol.* **2022**, *88*, 349–357. [CrossRef]
2. Peralta-Ruiz, Y.; Rossi, C.; Grande-Tovar, C.D.; Chaves-López, C.; Peralta-Ruiz, Y.; Rossi, C.; Grande-Tovar, C.D.; Chaves-López, C. Green Management of Postharvest Anthracnose Caused by *Colletotrichum gloeosporioides*. *J. Fungi* **2023**, *9*, 623. [CrossRef]
3. Rodríguez-Velázquez, N.D.; Gómez-de la Cruz, I.; López-Guillen, G.; Chávez-Ramírez, B.; Estrada-de los Santos, P. Isolation and Biological Control of *Colletotrichum* Sp. Causing Anthracnosis in *Theobroma Cacao* L. in Chiapas, Mexico. *J. Fungi* **2025**, *11*, 312. [CrossRef] [PubMed]
4. Meng, F.; Zhang, M. Advances in Functional Genomics Research on Appressorium Formation in *Colletotrichum gloeosporioides*. *Plant Pathol.* **2025**, *74*, 1519–1526. [CrossRef]
5. Chethana, K.W.T.; Jayawardena, R.S.; Chen, Y.J.; Konta, S.; Tibpromma, S.; Abeywickrama, P.D.; Gomdola, D.; Balasuriya, A.; Xu, J.; Lumyong, S.; et al. Diversity and Function of Appressoria. *Pathogens* **2021**, *10*, 746. [CrossRef]
6. Law, C.X.; Hashim, N.; Ismail, S.I.; Jahari, M.; Al Riza, D.F. A Review on Anthracnose Disease Caused by *Colletotrichum* Spp. in Fruits and Advances in Control Strategies. *Int. J. Food Microbiol.* **2025**, *442*, 111397. [CrossRef]
7. Ayón Reyna, L.E.; Uriarte Gastelum, Y.G.; Camacho Díaz, B.H.; Tapia Maruri, D.; López López, M.E.; López Velázquez, J.G.; Vega García, M.O. Antifungal Activity of a Chitosan and Mint Essential Oil Coating on the Development of *Colletotrichum Gloeosporioides* in Papaya Using Macroscopic and Microscopic Analysis. *Food Bioproc. Tech.* **2022**, *15*, 368–378. [CrossRef]
8. López-Bermúdez, L.S.; Quintana-Obregón, E.A.; Rosas-Burgos, E.C.; Gálvez-Iriqui, A.C.; Gutiérrez-Martínez, P.; Lizardi-Mendoza, J.; Plascencia-Jatomea, M. Acute Phytotoxicity and Antifungal Effect of Nanochitosan Particles on *Colletotrichum* Fructicola with Low Susceptibility to Chitosan. *Curr. Microbiol.* **2024**, *81*, 445. [CrossRef]
9. Gálvez-Iriqui, A.C.; Plascencia-Jatomea, M.; Bautista-Baños, S. Lysozymes: Characteristics, Mechanism of Action and Technological Applications on the Control of Pathogenic Microorganisms. *Rev. Mex. Fitopatol. Mex. J. Phytopathol.* **2020**, *38*, 360–383. [CrossRef]
10. Bilal, M.; Iqbal, H.M.N. Naturally-Derived Biopolymers: Potential Platforms for Enzyme Immobilization. *Int. J. Biol. Macromol.* **2019**, *130*, 462–482. [CrossRef] [PubMed]
11. Jiang, L.; Li, Y.; Wang, L.; Guo, J.; Liu, W.; Meng, G.; Zhang, L.; Li, M.; Cong, L.; Sun, M. Recent Insights Into the Prognostic and Therapeutic Applications of Lysozymes. *Front. Pharmacol.* **2021**, *12*, 767642. [CrossRef]
12. Wu, T.; Wu, C.; Fu, S.; Wang, L.; Yuan, C.; Chen, S.; Hu, Y. Integration of Lysozyme into Chitosan Nanoparticles for Improving Antibacterial Activity. *Carbohydr. Polym.* **2017**, *155*, 192–200. [CrossRef]
13. Wang, Y.; Li, S.; Jin, M.; Han, Q.; Liu, S.; Chen, X.; Han, Y. Enhancing the Thermo-Stability and Anti-Bacterium Activity of Lysozyme by Immobilization on Chitosan Nanoparticles. *Int. J. Mol. Sci.* **2020**, *21*, 1635. [CrossRef]
14. Zhang, H.; Feng, M.; Chen, S.; Shi, W.; Wang, X. Incorporation of Lysozyme into Cellulose Nanocrystals Stabilized β-Chitosan Nanoparticles with Enhanced Antibacterial Activity. *Carbohydr. Polym.* **2020**, *236*, 115974. [CrossRef]
15. Thanh, L.T.H.; Van Thanh, D.; Tue, N.H.; Hoa, P.T.B.; Tien, N.Q.D.; Loc, N.H. Antifungal Efficacy of Thermostable I168L Chitinase-ZnONPs Encapsulated in Alginate for Postharvest Fruit Storage. *Int. J. Biol. Macromol.* **2025**, *333*, 148991. [CrossRef] [PubMed]
16. Wu, T.; Jiang, Q.; Wu, D.; Hu, Y.; Chen, S.; Ding, T.; Ye, X.; Liu, D.; Chen, J. What Is New in Lysozyme Research and Its Application in Food Industry? A Review. *Food Chem.* **2019**, *274*, 698–709. [CrossRef] [PubMed]
17. Hernández-López, N.A.; Plascencia-Jatomea, M.; Del-Toro-Sánchez, C.L.; López-Saiz, C.M.; Morales-Rodríguez, S.; Martínez-Téllez, M.Á.; Quintana-Obregón, E.A. Antifungal Activity of Nanochitosan in *Colletotrichum* Musae and *Colletotrichum* Chrysophillum. *Polysaccharides* **2025**, *6*, 4. [CrossRef]
18. Hernández-López, N.A.; Plascencia-Jatomea, M.; Lizardi-Mendoza, J.; Martínez-Téllez, M.Á.; López-Saiz, C.M.; Quintana-Obregón, E.A. New Observations in the Spores and Hyphae of *Colletotrichum* Siamense Exposed to Nanochitosan Particles. *Arch. Microbiol.* **2025**, *207*, 260. [CrossRef]
19. Hernández-Téllez, C.N.; Cortez-Rocha, M.O.; Burgos-Hernández, A.; Rosas-Burgos, E.C.; Lizardi-Mendoza, J.; Torres-Arreola, W.; Burboa-Zazueta, M.G.; Plascencia-Jatomea, M. Chitosan/Carrageenan/Lysozyme Particles: Synthesis, Characterization and Antifungal Activity against Aspergillus Parasiticus. *Rev. Mex. Ing. Quim.* **2018**, *17*, 897–912. [CrossRef]

20. Shi, H.; Wen, H.; Xie, S.; Li, Y.; Chen, Y.; Liu, Z.; Jiang, N.; Qiu, J.; Zhu, X.; Lin, F.; et al. Antifungal Activity and Mechanisms of AgNPs and Their Combination with Azoxystrobin against Magnaporthe Oryzae. *Environ. Sci. Nano* **2023**, *10*, 2412–2426. [CrossRef]
21. Lopez-Moya, F.; Martin-Urdiroz, M.; Oses-Ruiz, M.; Were, V.M.; Fricker, M.D.; Littlejohn, G.; Lopez-Llorca, L.V.; Talbot, N.J. Chitosan Inhibits Septin-Mediated Plant Infection by the Rice Blast Fungus Magnaporthe Oryzae in a Protein Kinase C and Nox1 NADPH Oxidase-Dependent Manner. *New Phytol.* **2021**, *230*, 1578–1593. [CrossRef]
22. Valenzuela-Ortiz, G.; Gaxiola-Camacho, S.M.; San-Martín-hernández, C.; Martínez-Téllez, M.Á.; Aispuro-Hernández, E.; Lizardi-Mendoza, J.; Quintana-Obregón, E.A. Chitosan Sensitivity of Fungi Isolated from Mango (*Mangifera Indica* L.) with Anthracnose. *Molecules* **2022**, *27*, 1244. [CrossRef]
23. Rinaudo, M.; Milas, M.; Dung, P. Le Characterization of Chitosan. Influence of Ionic Strength and Degree of Acetylation on Chain Expansion. *Int. J. Biol. Macromol.* **1993**, *15*, 281–285. [CrossRef]
24. Rosas-Durazo, A.; Lizardi, J.; Higuera-Ciapara, I.; Argüelles-Monal, W.; Goycoolea, F.M. Development and Characterization of Nanocapsules Comprising Dodecyltrimethylammonium Chloride and κ-Carrageenan. *Colloids Surf. B Biointerfaces* **2011**, *86*, 242–246. [CrossRef]
25. Shugar, D. The Measurement of Lysozyme Activity and the Ultra-Violet Inactivation of Lysozyme. *Biochim. Biophys. Acta* **1952**, *8*, 302–309. [CrossRef]
26. Kim, M.; Park, M.; Jeong, Y. Purification and Characterization of Lysozyme from Filipino Venus, Ruditapes Philippinarum. *Food Sci. Biotechnol.* **2012**, *21*, 1463–1468. [CrossRef]
27. Noreen, S.; Pervaiz, F.; Ashames, A.; Buabeid, M.; Fahelelbom, K.; Shoukat, H.; Maqbool, I. Optimization of Novel Naproxen-Loaded Chitosan/Carrageenan Nanocarrier-Based Gel for Topical Delivery: Ex Vivo, Histopathological, and In Vivo Evaluation. *Pharmaceuticals* **2021**, *14*, 557. [CrossRef]
28. Rubina, M.; Elmanovich, I.; Vasil'kov, A. AFM Studies of Chitosan, Gold-Chitosan, and Silver-Chitosan Films Morphology. *Macromol. Symp.* **2020**, *389*, 1900068. [CrossRef]
29. Sigma-Aldrich Drug Delivery FAQs. Available online: https://www.sigmaaldrich.com/MX/es/technical-documents/technical-article/materials-science-and-engineering/drug-delivery/drug-delivery-questions (accessed on 21 July 2025).
30. Gálvez-Iriqui, A.C.; Cortez-Rocha, M.O.; Burgos-Hernández, A.; Calderón-Santoyo, M.; Argüelles-Monal, W.M.; Plascencia-Jatomea, M. Synthesis of Chitosan Biocomposites Loaded with Pyrrole-2-Carboxylic Acid and Assessment of Their Antifungal Activity against Aspergillus Niger. *Appl. Microbiol. Biotechnol.* **2019**, *103*, 2985–3000. [CrossRef]
31. Varan, N.Y. Characterization of Chitosan Particles via Attenuated Total Reflection Fourier Transform Infrared Spectroscopy, Conductometric Titration, Viscosity Average Molecular Weight and X-Ray Photoelectron Spectroscopy. *Asian J. Chem.* **2017**, *29*, 825–828. [CrossRef]
32. Zhu, W.; Xu, X.; Peng, F.; Yan, D.Z.; Zhang, S.; Xu, R.; Wu, J.; Li, X.; Wei, W.; Chen, W. The Cyclase-Associated Protein ChCAP Is Important for Regulation of Hyphal Growth, Appressorial Development, Penetration, Pathogenicity, Conidiation, Intracellular CAMP Level, and Stress Tolerance in *Colletotrichum* Higginsianum. *Plant Sci.* **2019**, *283*, 1–10. [CrossRef]
33. Thambiliyagodage, C.; Jayanetti, M.; Mendis, A.; Ekanayake, G.; Liyanaarachchi, H.; Vigneswaran, S. Recent Advances in Chitosan-Based Applications—A Review. *Materials* **2023**, *16*, 2073. [CrossRef]
34. Carrera, C.; Bengoechea, C.; Carrillo, F.; Calero, N. Effect of Deacetylation Degree and Molecular Weight on Surface Properties of Chitosan Obtained from Biowastes. *Food Hydrocoll.* **2023**, *137*, 108383. [CrossRef]
35. Emolaga, C.S.; Milo, L.C.; Basilia, B.A. Size-Directed Preparation of Chitosan-Carrageenan Nanoparticles Using Dynamic Light Scattering for Sustainable Materials Development. *Sustain. Chem. One World* **2025**, *7*, 100091. [CrossRef]
36. Kumar, R.; Najda, A.; Duhan, J.S.; Kumar, B.; Chawla, P.; Klepacka, J.; Malawski, S.; Sadh, P.K.; Poonia, A.K. Assessment of Antifungal Efficacy and Release Behavior of Fungicide-Loaded Chitosan-Carrageenan Nanoparticles against Phytopathogenic Fungi. *Polymers* **2022**, *14*, 41. [CrossRef]
37. Đekić, L.; Ćirić, A. Polyelectrolyte Complexes of Chitosan as Potential Drug Delivery Systems. In *Chitosan-Based Drug Delivery Systems*; Sougata, J., Ed.; Springer: Cham, Switzerland, 2025; Volume 16, pp. 59–92, ISBN 978-3-032-08347-0.
38. Ramos, J.; Laux, V.; Mason, S.A.; Lemée, M.H.; Bowler, M.W.; Diederichs, K.; Haertlein, M.; Forsyth, V.T.; Mossou, E.; Larsen, S.; et al. Structure and Dynamics of the Active Site of Hen Egg-White Lysozyme from Atomic Resolution Neutron Crystallography. *Structure* **2025**, *33*, 136–148. [CrossRef]
39. Kumari, M.; Singh, U.K.; Beg, I.; Alanazi, A.M.; Khan, A.A.; Patel, R. Effect of Cations and Anions of Ionic Liquids on the Stability and Activity of Lysozyme: Concentration and Temperature Effect. *J. Mol. Liq.* **2018**, *272*, 253–263. [CrossRef]
40. Nishimoto, E.; Yamashita, S.; Yamasaki, N.; Imoto, T. Resolution and Characterization of Tryptophyl Fluorescence of Hen Egg-White Lysozyme by Quenching- and Time-Resolved Spectroscopy. *Biosci. Biotechnol. Biochem.* **1999**, *63*, 329–336. [CrossRef]
41. Putro, J.N.; Lunardi, V.B.; Soetaredjo, F.E.; Yuliana, M.; Santoso, S.P.; Wenten, I.G.; Ismadji, S. A Review of Gum Hydrocolloid Polyelectrolyte Complexes (PEC) for Biomedical Applications: Their Properties and Drug Delivery Studies. *Processes* **2021**, *9*, 1796. [CrossRef]

42. Ren, D.; Yi, H.; Wang, W.; Ma, X. The Enzymatic Degradation and Swelling Properties of Chitosan Matrices with Different Degrees of N-Acetylation. *Carbohydr. Res.* **2005**, *340*, 2403–2410. [CrossRef]
43. Filippov, S.K.; Khusnutdinov, R.; Murmiliuk, A.; Inam, W.; Zakharova, L.Y.; Zhang, H.; Khutoryanskiy, V.V. Dynamic Light Scattering and Transmission Electron Microscopy in Drug Delivery: A Roadmap for Correct Characterization of Nanoparticles and Interpretation of Results. *Mater. Horiz.* **2023**, *10*, 5354–5370. [CrossRef]
44. Madihalli, S.; Masti, S.P.; Eelager, M.P.; Gunaki, M.N.; Chougale, R.B.; Dalbanjan, N.P.; Praveen Kumar, S.K. Fabrication and Characterization of Methylcellulose/Chitosan Active Films Incorporated with l -Arginine and Their Potential in the Green Packaging of Grapes. *Sustain. Food Technol.* **2025**, *3*, 1035–1052. [CrossRef]
45. Ballard, E.; Yucel, R.; Melchers, W.J.G.; Brown, A.J.P.; Verweij, P.E.; Warris, A. Antifungal Activity of Antimicrobial Peptides and Proteins against Aspergillus Fumigatus. *J. Fungi* **2020**, *6*, 65. [CrossRef]
46. Domnin, M.; Aslanli, A.; Senko, O.; Stepanov, N.; Efremenko, E. Enzymes Degrading Fungal Cell Wall Components vs. Those Exhibiting Lactonase Activity as Participants of Antifungals. *Sci* **2025**, *7*, 169. [CrossRef]
47. Chen, S.; Wang, Y.; Schnabel, G.; Peng, C.A.; Lagishetty, S.; Smith, K.; Luo, C.; Yuan, H. Inherent Resistance to 14α-Demethylation Inhibitor Fungicides in *Colletotrichum* Truncatum Is Likely Linked to CYP51A and/or CYP51B Gene Variants. *Phytopathology* **2018**, *108*, 1263–1275. [CrossRef]
48. Ing, L.Y.; Zin, N.M.; Sarwar, A.; Katas, H. Antifungal Activity of Chitosan Nanoparticles and Correlation with Their Physical Properties. *Int. J. Biomater.* **2012**, *2012*, 632698. [CrossRef]
49. Xing, Y.; Yi, R.; Yang, H.; Xu, Q.; Huang, R.; Tang, J.; Li, X.; Liu, X.; Wu, L.; Liao, X.; et al. Antifungal Effect of Chitosan/Nano-TiO_2 Composite Coatings against *Colletotrichum gloeosporioides*, *Cladosporium oxysporum* and *Penicillium steckii*. *Molecules* **2021**, *26*, 4401. [CrossRef]
50. Lopez-Moya, F.; Suarez-Fernandez, M.; Lopez-Llorca, L.V. Molecular Mechanisms of Chitosan Interactions with Fungi and Plants. *Int. J. Mol. Sci.* **2019**, *20*, 332. [CrossRef]
51. Walker, G.M.; White, N.A. Introduction to Fungal Physiology. In *Fungi: Biology and Applications*; John Wiley & Sons: Hoboken, NJ, USA, 2017; pp. 1–35. [CrossRef]
52. Harris, S.D. Duplicating the Mold: Branching of Fungal Hyphae. *Fungal Genet. Biol.* **2025**, *180*, 104025. [CrossRef]
53. Harris, S.D. Hyphal Branching in Filamentous Fungi. *Dev. Biol.* **2019**, *451*, 35–39. [CrossRef]
54. He, P.; Wang, Y.; Wang, X.; Zhang, X.; Tian, C. The Mitogen-Activated Protein Kinase CgMK1 Governs Appressorium Formation, Melanin Synthesis, and Plant Infection of *Colletotrichum gloeosporioides*. *Front. Microbiol.* **2017**, *8*, 302320. [CrossRef]
55. Shen, Z.F.; Li, L.; Zhu, X.M.; Liu, X.H.; Klionsky, D.J.; Lin, F.C. Current Opinions on Mitophagy in Fungi. *Autophagy* **2023**, *19*, 747–757. [CrossRef]
56. Dharma, K.S.; Suryanti, S.; Widiastuti, A. Hormesis in Pathogenic and Biocontrol Fungi: From Inhibition to Stimulation. *Caraka Tani J. Sustain. Agric.* **2024**, *39*, 281–296. [CrossRef]
57. Song, J.; Han, C.; Zhang, S.; Wang, Y.; Liang, Y.; Dai, Q.; Huo, Z.; Xu, K. Hormetic Effects of Carbendazim on Mycelial Growth and Aggressiveness of Magnaporthe Oryzae. *J. Fungi* **2022**, *8*, 1008. [CrossRef]
58. Hu, S.; Li, J.; Wang, P.; Zhu, F. Hormetic Effects of Dimethachlone on Mycelial Growth and Virulence of Sclerotinia Sclerotiorum. *Phytopathology* **2021**, *111*, 1166–1172. [CrossRef]
59. Palma-Guerrero, J.; Larriba, E.; Güerri-Agulló, B.; Jansson, H.B.; Salinas, J.; Lopez-Llorca, L.V. Chitosan Increases Conidiation in Fungal Pathogens of Invertebrates. *Appl. Microbiol. Biotechnol.* **2010**, *87*, 2237–2245. [CrossRef] [PubMed]
60. Deng, Z.Q.; Wang, D.; de Mou, Q.; Liu, L.Y.; Li, Y.; Lu, T.; Chen, W.R.; Xie, X.S.; Bao, A.L.; Tang, X.R.; et al. Antifungal Activity of Novel 5,6,7,8-Tetrahydroquinazolin Derivatives against Plant Pathogenic Fungi by Targeting Sterol 14α-Demethylase (CYP51) and the Application on Rice. *J. Agric. Food Chem.* **2025**, *73*, 24392–24403. [CrossRef] [PubMed]
61. Akosah, Y.A.; Kostennikova, Z.S.; Lutfullin, M.T.; Lutfullina, G.F.; Afordoanyi, D.M.; Vologin, S.G.; Mardanova, A.M. Induced Expression of CYP51a and HK1 Genes Associated with Penconazole and Fludioxonil Resistance in the Potato Pathogen Fusarium Oxysporum. *Microorganisms* **2023**, *11*, 1257. [CrossRef]

Disclaimer/Publisher's Note: The statements, opinions and data contained in all publications are solely those of the individual author(s) and contributor(s) and not of MDPI and/or the editor(s). MDPI and/or the editor(s) disclaim responsibility for any injury to people or property resulting from any ideas, methods, instructions or products referred to in the content.